Faculdade de Engenharia da Universidade do Porto

The Analysis of Reinforced Structures Considering a Damage Model: a Meshless Approach

José Manuel Vicente Berardo

FINAL VERSION

Dissertation carried out under the
Master in Computational Mechanics

Supervisor: Prof. Dr. Jorge A. O. P. Belinha
Other Supervisors: Prof. Dr. Francisco M. A. Pires
Prof. Dr. Rui M. M. Carneiro de Barros

October 2015

THIS PAGE INTENTIONALLY LEFT IN BLANK

Abstract

In this work, first, the radial point interpolation method (RPIM) is extended to the elasto-static analysis of circular plates using the 2D axisymmetric deformation theory.

After that, using the RPIM, a rate-independent isotropic damage model developed for the numerical analysis of concrete subjected to prescribed displacements is presented. This model is also implemented for the numerical analysis of reinforced concrete beam environment. The RPIM in the present methodology is used to obtain the strain and stress fields. The RPIM is a meshless method whose shape functions possess the Kronecker delta property, assuring an interpolating process. The constitutive model adopted is mostly from one source (Cervera, Oliver, and Manzoli 1996), isotropic rate-independent damage model. This model uses the split of the stress tensor in compression and tension in order to obtain the compressive and tensile damage coefficients. This model is appropriate to predict the damage behavior of concrete. Several examples are analyzed and the obtained results are in agreement with the literature.

THIS PAGE INTENTIONALLY LEFT IN BLANK

Acknowledges

I wish to sincerely thank the invaluable help of my dear supervisor, Professor Jorge Belinha. Without his contribution, key steps would hardly be unlocked. It is well known his extensive experience in meshless methods, a main subject of this work.

I also want to thank my dear supervisor Professor Francisco Pires for his crucial tips within the damage model theory, subject he has remarkable experience.

Many thanks to my dear supervisor Professor Rui Carneiro de Barros following his tremendous help regarding the sharing of his extensive years' experience in reinforced concrete structures towards this work.

I need to mention, with enormous thankyou to dear professor José César de Sá for his incredible availability for any kind of help or theoretical guidance throughout all the master's program. Particularly, as a trivial example, this work needed computing capacity above I could ever provide by my means, but was made possible because of your good will providing me a temporary machine.

THIS PAGE INTENTIONALLY LEFT IN BLANK

Table of Contents

List of Figures

List of Tables

1. Introduction

An accurate way to predict the behavior of structural components made of commonly used materials has been always a reason for a quest for many areas of engineering sciences (Bazant 2010). Different numerical discrete methods have been used extensively over several decades. No doubt exists that *Finite Element Method* (*FEM*) is the most widely commercially used. But do exist alternatives. And other methods may do better. In any kind of method, one always will find some kind of frontier that lead to a limitation. Some occasions that struggle leads to a desirable improvement. But there are cases where it is not possible to find a direct suitable solution for that obstacle. As a clue, many of us wished the discretization of some complex geometries would be made with less restricting rules. Actually more and more often, simulations need to be made based on large deformations or are time/rate dependent with drastic geometric changes within the load steps. One of the most needed things are re-mesh algorithms that may not be dependent of human interaction in every time-step increment. Well, this work addresses a numerical method that is not just an alternative but it has all characteristics to be soon the first choice in many applications. Such method it is a Meshless Method, the *Radial Point Interpolation Method*, *RPIM*.

RPIM has been proven to be a way to accurately predict the material behavior, in linear elastic, elastoplastic and in many other nonlinear regimes. Regarding this meshless method we may recall it is a very flexible method. It needs a relatively easy 'background' Gaussian integration mesh just covering the whole geometry. In that

mesh, for example, we don't need to worry with hanging nodes like we would need in FEM for elements discretization. In RPIM, after that it is necessary to implement any common available nodal mesh generation scheme in order to discretize the geometry. And at this point it is easily overcame what other non-meshless methods may frequently fail to do, a suitable geometric problem discretization. This means that at least a door for analyzing, for example, some crash event, an explosion or any complex geometrical problems is open to pass through with RPIM. But the RPIM doesn't end with discretization itself. Actually, it's the fairly starting point. Further RPIM related implementation setup and theoretical fundaments are thoroughly presented in ***Chapter 2*** (Farahani et al. 2015), ***Radial Point Interpolation Method***, namely their subsections covering distinct themes as *Nodal Connectivity and Numerical integration* and *Radial Point Interpolators.*

If equivalent results are possible to compute from any two different methods, all industrial investors will prefer the method which is faster or the one which needs less economical resources. One of the most common real-life 3D geometry shapes are the ones we may consider axisymmetric (Segall 1992). And if instead of a full 3D numerical discrete equations system approach we simplify it to an equivalent 2D problem, much cheaper, we will get positive business leaders attention as well. No previous work was known to be published in any journal till delivery of this thesis, about using RPIM in a detailed axisymmetric study. Given the recent interest in RPIM by many researchers and its potential for suitable commercial use, that seemed to be mostly opportune. Giving the relevant basic guidelines of the Axisymmetric Theory, first subsection of ***Chapter 3*** gives insight over ***Axisymmetric Discrete equation System*** (Farahani et al. 2015), also through *Variable Fields* (Farahani et al. 2015) and *Weak-form of Galerkin.* That detailed axisymmetric view gives support for the appropriate constitutive material matrix used in axisymmetric analyzes.

Two of the modern world marvels, let's say since 1853, are so much implemented that we are surrounded by both of them most of our lifetime. We don't think much about it, thankfully, due partially to large security margins required to its implementation. Such marvels are two of the structural solutions most used in civil construction, they are the concrete and the reinforced concrete beams. Frequently,

concrete beams and especially reinforced concrete beams are implemented in a prismatic shape, with rectangular cross section. Again if we want to make an exhaustive study, with several subtle incremental variable evolution, we may need to simplify the simulations cost. Also adding the fact we may need countless iterations or incremental steps if we want to address nonlinear material model laws. Given those characteristics, one suitable and well known way to overcame that, is through another 2D equivalent deformation theory used in *Continuum Mechanics*: is the *Plane Stress* approach, which can be used for this extruded-like geometry, beams. This simple but, yet important, method is addressed in ***Chapter 3***, namely in subsections ***Plane Stress Discrete Equation System*** and *Constitutive Equations.*

But the intent of this work in using concrete material goes way farthest from just simple elastic analyzes. It is widely known the extent use of safety factors that are present in the most basic and important rules of *European Union, EU,* the *Eurocodes.* There are some disadvantages in *Eurocodes*, for example the over dimensioning of structures, that could be improved though newer and reliable numerical methods. We can say that prediction of actually failure point, or degradation evolution are the present cutting edge knowledge 'weapon' in an economical competitive business world. And concrete is, rather than 'just' crucial, but is also a material with an intriguing particular behavior, challenging any model implementation attempt. If compressed tends to be somehow apparently 'stable' with a ductile degradative behavior. But when we traction it, show, after lower yield regimes than compression, a brittle behavior (sudden cracks and easily fails entirely). Given the so many reasons we can think of, whether we like it or not, concrete deserves exhaustive attention. With that in mind, some authors have been using a theory that seems to fit into observational experiments of concrete or reinforced concrete. *Continuum Damage Mechanics Theory*, *CDMT*, it is such theory. This *CDMT* mostly addresses numerical solution schemes for material degradation evolution laws. And the particular theory used in this work and the reasons of doing so, are addressed in ***Chapter 4***, ***Nonlinear Mechanics: Damage*** (Cervera, Oliver, and Manzoli 1996) and its subsection *Multidimensional Rate-Independent Model*. Some reasoned adaptive choices were made to accommodate the damage model, given it is a

model initially developed for other methods, like the *FEM* and not firstly intended for *RPIM*.

Some particular challenging setup issues within this work showed up in one punctual non correlation from *FEM*, namely the mesh *characteristic length*. But for engineers from *Computational Mechanics* field, it is easy to embrace those difficulties as part of a symbolic drawing board or part of a computational laboratory work both grueling and exciting. Still, some future work should address this subject in more detail.

As a starting point, several exhaustive studies were performed in elastic axisymmetric plates, in ***Chapter 5***, *Numerical Examples*, specifically in subsection ***Circular Plate under Uniform Distributed Load*** (Farahani et al. 2015). Isolated variables were systematically studied so their influence could be undeniably captured more reasonably. This set of studies were so crucial for RPIM validation and showed a remarkable outcome in that sense.

The first nonlinear model example, of the *Isotropic Rate-Independent Damage Model*, was analyzed 'alone' in one plain concrete beam. These was convenient because allowed a more isolation of all law behavior effects and made so a more controlled routine environment. An exhaustive convergence study was performed showing that the model routine was properly implemented. This is presented in detail in ***Chapter 5***, *Numerical Examples* specifically in subsection ***Plain Concrete Beam under Three Point Bend Test*** (Cervera, Oliver, and Manzoli 1996). The results show an undeniable converged state in magnitude and shape with respect to evolution of load-displacement curves. This example settled the necessary, validated, confidence in the implemented damage model to advance to a further much demanding example, reinforced concrete.

All of this thesis numerical work was not performed in a fully ready to use, commercial available *RPIM* software. But instead, a *Matlab* code with RPIM implemented by *Professor Jorge Belinha*, with elastoplastic capabilities, was used here. Given that, it was initially intended to reproduce some example that also could address plasticity of reinforced concrete, where plasticity would be implemented just within the equivalent reinforcement bar and damage would be implemented just within the concrete. But not all examples available in the literature have fully suitable and available

data parameters that are needed to accurately implement the present chosen damage or plasticity models. Finally the experimental example that was used, for reinforced concrete, didn't have a reinforced material, rebar, with the elastoplastic behavior. Instead the material have the elastic-failure behavior and it is called *Glass Fiber Reinforced Polymer,* or *GFRP*. This is addressed in ***Chapter 5***, *Numerical Examples,* under the subsection *reinforced* ***Concrete Beam under Four Point Loading Test*** (Metwally 2015). The results show very close load-deflection curve shape and magnitude when compared with experimental data. The Damage Model was double satisfactorily validated with more this key remarkable example.

This work is the culmination of a sweet journey I started two years ago, with the beginning of these unique *Computational Mechanics Master* in ***FEUP***. Within it I learned so much more than I first imagined. But today I see that exists countless related subjects I would love to academically or professionally pursue, if was possible. But at least some of them I believe I will.

2. Radial Point Interpolation Method

"The meshless method applied in this work is the Radial Point Interpolation Method (Wang and Liu 2002a) (Wang and Liu 2002b) (Belinha 2014) (RPIM). The RPIM is an interpolator meshless method which uses the concept of influence-domain to force the nodal connectivity. To numerically integrate the integro-differential equations governing the physical phenomenon, the RPIM uses a background integration mesh constructed using integration cells and the Gauss-Legendre quadrature rule" (Farahani et al. 2015).

2.1. Nodal Connectivity and Numerical Integration

"Several meshless methods use the concept of influence-domain due to its simplicity" (Farahani et al. 2015).

"The meshless methods are discrete numerical methods, such as the Finite Element Method (FEM). However, instead of discretizing the problem domain in elements and nodes, meshless methods discretize the problem domain only using nodes or points"(Farahani et al. 2015).

"The predefined finite element mesh assures the nodal connectivity in the FEM. The nodes belonging to the same element interact directly between each other and with the boundary nodes of neighbour finite elements. In opposition, since there is no predefined nodal interdependency, in meshless methods the nodal connectivity is determined after the nodal discretization (Belinha 2014), being obtained by the overlap of the influence-domain of each node. These influence-domains can be determined by searching radially enough nodes inside a fixed area or a fixed volume, respectively for the 2D problem and for the 3D problem. Because of its simplicity many meshless methods use this concept (Belytschko, Lu, and Gu 1994) (W. K. Liu, Jun, and Zhang 1995) (Atluri and Zhu 1998) (Wang and Liu 2002a) (Nguyen et al. 2008) (Belinha 2014). However, the size or shape variation of these influence-domains along the problem domain affects the performance and the final solution of the meshless method. It is important that all the influence domains in the problem contain approximately the same number of nodes. Irregular domain boundaries or node clusters in the nodal mesh can lead to unbalanced influence-domains (Belinha 2014). Regardless the used meshless technique, previous works suggest that each 2D influence-domain should possess between $n=[9,16]$ nodes (Belytschko, Lu, and Gu 1994) (W. K. Liu, Jun, and Zhang 1995) (Atluri and Zhu 1998) (Wang and Liu 2002a) (Nguyen et al. 2008) (Belinha 2014)" (Farahani et al. 2015).

"In discrete numerical methods using a variational formulation, such as the Galerkin weak formulation, the numerical integration process, required to determine the system of equations based on the integro-differential equations ruling the studied

physical phenomenon, represents a significant percentage of the total computational cost of the analysis. In the FEM the integration mesh is coincident with the element mesh. Since the FEM shape functions are known polynomial functions, the number of integration points per integration cell can be pre-determined using accurate well-known relations (Zienkiewicz and Taylor 1994) (Bathe 1982). In meshless methods the shape function degree is generally unknown, thus it is not possible to accurately define a priori the background integration mesh" (Farahani et al. 2015).

"The numerical integration scheme used in this work follows the suggestion of previous RPIM works (Wang and Liu 2002a) (Wang and Liu 2002b). The solid domain is divided in a regular grid forming quadrilateral integration cells. Then, each grid-cell is filled with integration points, respecting the Gauss-Legendre quadrature rule (Belinha 2014)" (Farahani et al. 2015).

"In the literature it is possible to find several works using the RPIM, however the state-of-art lacks some detailed studies on the RPIM combined with the axisymmetric deformation theory. Thus, in this work a sample of a full axisymmetric-RPIM calibration study is performed, from another work already submitted (Farahani et al. 2015), in order to determine: the optimal number of nodes forming each influence-domain and; the most accurate spatial disposition of the integration cells, and respective integration order" (Farahani et al. 2015).

2.2. Radial Point Interpolators

"The RPIM shape functions are obtained using the Radial Point Interpolators (RPI), which combine radial basis functions with polynomial basis functions. Thus, consider a function space T defined in the analysed domain $\Omega \subset \Re^d$. The finite dimensional space $T_h \subset T$ discretising the domain Ω is defined by: $T_h := \langle r(x-x_i) : i \in \Re \wedge i \leq N \rangle + p_m(x)$, where $r : \Re^d \mapsto \Re$ is at least a C^1-function and $p_m : \Re^d \mapsto \Re$ is defined in the space of polynomials of degree less than m. In this work only simplified two-dimensional domains $\Omega \subset \Re^2$ are studied, therefore it is consider an interpolation function $u^h(\boldsymbol{x})$ defined in an influence-domain $\Omega_I \subset \Omega$ of an interest point $x_I \in \Re^2$ and discretised by set of N arbitrarily distributed nodes $\boldsymbol{N}_I = \{n_1, n_2, ..., n_N\}$. The nodal set is defined in the two-dimensional space by $X = \{x_1, x_2, ..., x_N\} \wedge x_i \in \Re^2$, being n the number of nodes in the influence-domain of $\boldsymbol{x}_I$. The density of $\boldsymbol{X}$ is identified by h,

$$h = \min \left\| x_j - x_i \right\|, \forall \{i, j\} \in \mathrm{N} : \{i, j\} \leq N \wedge i \neq j \qquad \textbf{2-1}$$

being $\| \cdot \|$ the Euclidean norm" (Farahani et al. 2015).

"The RPI constructs the interpolation function $u^h(\boldsymbol{x}) \in T$ capable to pass through all nodes within the influence-domain, meaning that since the nodal function value is assumed to be u_i at the node $\boldsymbol{x}_i$, $u_i = u(\boldsymbol{x}_i)$, consequently $u^h(\boldsymbol{x}_i) = u(\boldsymbol{x}_i)$. Using a radial basis function $r(\boldsymbol{x})$ and polynomial basis function $p(\boldsymbol{x})$, the interpolation function $u^h(\boldsymbol{x}) \in T$ can be defined at the interest point $x_I \in \Re^2$ (not necessarily coincident with any $\boldsymbol{x}_i \in \boldsymbol{X}$) by" (Farahani et al. 2015),

$$u^h(\boldsymbol{x}_I) = \sum_{i=1}^{n} r_i(\boldsymbol{x}_I) a_i + \sum_{j=1}^{m} p_j(\boldsymbol{x}_I) b_j = \boldsymbol{r}(\boldsymbol{x}_I)^{\mathrm{T}} \boldsymbol{a} + \boldsymbol{p}(\boldsymbol{x}_I)^{\mathrm{T}} \boldsymbol{b} = u(\boldsymbol{x}_I) \qquad \textbf{2-2}$$

"Where a_i is the non-constant coefficient of $r_i(\boldsymbol{x}_I)$ and b_j the non-constant coefficient for $p_j(\boldsymbol{x}_I)$. The integer n is the number of nodes inside the influence-domain of the interest point $\boldsymbol{x}_I$. The vectors are defined as,

$$\boldsymbol{a}^{\mathrm{T}} = \{a_1, a_2, ..., a_n\} \quad \textbf{2-3}$$

$$\boldsymbol{b}^{\mathrm{T}} = \{b_1, b_2, ..., b_m\} \quad \textbf{2-4}$$

$$\boldsymbol{r}(\boldsymbol{x})^{\mathrm{T}} = \{r_1(\boldsymbol{x}), r_2(\boldsymbol{x}), ..., r_n(\boldsymbol{x})\} \quad \textbf{2-5}$$

$$\boldsymbol{p}(\boldsymbol{x})^{\mathrm{T}} = \{p_1(\boldsymbol{x}), p_2(\boldsymbol{x}), ..., p_m(\boldsymbol{x})\} \quad \textbf{2-6}$$

being $\boldsymbol{x}_i = \{x_i, y_i\}$. This work uses the Multiquadrics Radial Basis Function (MQ-RBF) (Wang and Liu 2002a) (Wang and Liu 2002b) (Belinha 2014), which can be defined by $\boldsymbol{r}_i(\boldsymbol{x}_I) = \boldsymbol{s}(d_{iI}) = \left(d_{iI}^2 + c^2\right)^p$, where d_{iI} is a distance between the interest point $\boldsymbol{x}_I = \{x_I, y_I\}$ and the node $\boldsymbol{x}_i = \{x_i, y_i\}$, being $d_{iI} = \sqrt{(x_i - x_I)^2 + (y_i - y_I)^2}$. The c and p variables are the MQ-RBF shape parameters, which are fixed values determined in previous works (Wang and Liu 2002a) (Wang and Liu 2002b). The variation of these parameters can affect the performance of the MQ-RBFs. In the work of Wang and Liu (Wang and Liu 2002a) (Wang and Liu 2002b) it was shown that the optimal values are $c = 1.42$ and $p = 1.03$, which are the values used in this work. The original RPI formulation requires a complete polynomial basis function, which for the two-dimensional space can be defined by" (Farahani et al. 2015),

$$\boldsymbol{p}(\boldsymbol{x}_i)^{\mathrm{T}} = \{1, x_i, y_i, x_i^2, x_i y_i, y_i^2, ...\} \quad \textbf{2-7}$$

"However, it was shown in previous RPI research works (Belinha 2014) (L.M.J.S. Dinis, Natal Jorge, and Belinha 2007) (L. M J S Dinis, Natal Jorge, and Belinha 2008) that using a simple constant basis increases the RPI formulation efficiency. Thus, in this work only the constant basis is considered $\boldsymbol{p}(\boldsymbol{x}_i) = \{1\}$, for which the number of monomial

terms is defined by $m=1$. The coefficients a_i and b_j in equation 2-2 are determined by enforcing the interpolation to pass through all n nodes within the influence-domain (Belinha 2014). The interpolation at the k^{th} node is defined by" (Farahani et al. 2015),

$$u^h(x_k,y_k)=\sum_{i=1}^{n} r_i(x_k,y_k)a_i+\sum_{j=1}^{m} p_j(x_k,y_k)b_j=u_k,\quad k=1,2,\ldots,n \qquad \textbf{2-8}$$

"The inclusion of the following polynomial term is an extra-requirement that guarantees unique approximation (Belinha 2014) (L. M J S Dinis, Natal Jorge, and Belinha 2008)" (Farahani et al. 2015),

$$\sum_{i=1}^{n} p_j(x_i,y_i)a_i=0,\quad j=1,2,\ldots,m \qquad \textbf{2-9}$$

"The computation of the shape functions are written in a matrix form as" (Farahani et al. 2015)

$$\begin{bmatrix} \boldsymbol{R} & \boldsymbol{P} \\ \boldsymbol{P}^T & \boldsymbol{Z} \end{bmatrix}\begin{Bmatrix} \boldsymbol{a} \\ \boldsymbol{b} \end{Bmatrix}=\begin{Bmatrix} \boldsymbol{u} \\ \boldsymbol{z} \end{Bmatrix}\Leftrightarrow \boldsymbol{G}\begin{Bmatrix} \boldsymbol{a} \\ \boldsymbol{b} \end{Bmatrix}=\begin{Bmatrix} \boldsymbol{u} \\ \boldsymbol{z} \end{Bmatrix} \qquad \textbf{2-10}$$

"Where $\boldsymbol{G}$ is the complete moment matrix, $\boldsymbol{Z}$ is a null matrix defined by $Z_{ij}=0,\forall\{\{i,j\}\in \mathrm{N}:\{i,j\}\le m\}$ and the null vector $\boldsymbol{z}$ can be represented by $z_i=0,\forall\{i\in \mathrm{N}:i\le m\}$. The vector for function values is defined as $u_i=u(x_i),\forall\{i\in \mathrm{N}:i\le n\}$. The radial moment matrix $\boldsymbol{R}$ is represented as," (Farahani et al. 2015)

$$\underset{[n\times n]}{\boldsymbol{R}}=\begin{bmatrix} r_1(x_1,y_1) & r_1(x_2,y_2) & \cdots & r_1(x_n,y_n) \\ r_2(x_1,y_1) & r_2(x_2,y_2) & \cdots & r_2(x_n,y_n) \\ \vdots & \vdots & \ddots & \vdots \\ r_n(x_1,y_1) & r_n(x_2,y_2) & \cdots & r_n(x_n,y_n) \end{bmatrix} \qquad \textbf{2-11}$$

"And polynomial moment matrix $\boldsymbol{P}$ is defined as" (Farahani et al. 2015),

$$\underset{[n\times m]}{\boldsymbol{P}}=\begin{bmatrix} p_1(x_1,y_1) & p_2(x_1,y_1) & \cdots & p_m(x_1,y_1) \\ p_1(x_2,y_2) & p_2(x_2,y_2) & \cdots & p_m(x_2,y_2) \\ \vdots & \vdots & \ddots & \vdots \\ p_1(x_n,y_n) & p_2(x_n,y_n) & \cdots & p_m(x_n,y_n) \end{bmatrix} \qquad \textbf{2-12}$$

"Since the distance is directionless, $r_i(x_j, y_j) = r_j(x_i, y_i)$, i.e. $R_{ij} = R_{ji}$, matrix $\boldsymbol{R}$ is symmetric. A unique solution is obtained if the inverse of the radial moment matrix $\boldsymbol{R}$ exists" (Farahani et al. 2015),

$$\begin{Bmatrix} \boldsymbol{a} \\ \boldsymbol{b} \end{Bmatrix} = \boldsymbol{G}^{-1} \begin{Bmatrix} \boldsymbol{u} \\ \boldsymbol{z} \end{Bmatrix} \qquad \textbf{2-13}$$

"The solvability of this system is usually guaranteed by the requirements $rank(p) = m \leq n$ (Wang, Liu, and Wu 2001). In this work, the influence-domain will always possess enough nodes to largely satisfy the previously mentioned condition. It is possible to obtain the interpolation with

$$u^h(\boldsymbol{x}_I) = \left\{ \boldsymbol{r}(\boldsymbol{x}_I)^T ; \boldsymbol{p}(\boldsymbol{x}_I)^T \right\} \boldsymbol{G}^{-1} \begin{Bmatrix} \boldsymbol{u} \\ \boldsymbol{z} \end{Bmatrix} = \left\{ \Phi(\boldsymbol{x}_I)^T ; \Psi(\boldsymbol{x}_I)^T \right\} \begin{Bmatrix} \boldsymbol{u} \\ \boldsymbol{z} \end{Bmatrix} \qquad \textbf{2-14}$$

where the interpolation function vector $\Phi(\boldsymbol{x}_I)$ is defined by

$$\Phi(\boldsymbol{x}_I) = \left\{ \varphi_1(\boldsymbol{x}_I) \quad \varphi_2(\boldsymbol{x}_I) \quad \cdots \quad \varphi_n(\boldsymbol{x}_I) \right\} \qquad \textbf{2-15}$$

and the residual vector $\psi(\boldsymbol{x}_I)$, with no relevant physical meaning, is expressed as follows," (Farahani et al. 2015)

$$\Psi(\boldsymbol{x}_I) = \left\{ \psi_1(\boldsymbol{x}_I) \quad \psi_2(\boldsymbol{x}_I) \quad \cdots \quad \psi_m(\boldsymbol{x}_I) \right\} \qquad \textbf{2-16}$$

"Since

$$u^h(\boldsymbol{x}_I) = \Phi(\boldsymbol{x}_I)^T \boldsymbol{u} = \left\{ \Phi(\boldsymbol{x}_I)^T ; \Psi(\boldsymbol{x}_I)^T \right\} \begin{Bmatrix} \boldsymbol{u} \\ \boldsymbol{z} \end{Bmatrix} \qquad \textbf{2-17}$$

It is possible to obtain the partial derivatives of the interpolated field variable, with respect to a generic variable ξ which can be $\xi = x$ or $\xi = y$, with the following expression" (Farahani et al. 2015)

$$\frac{\partial u^h(\boldsymbol{x}_I)}{\partial \xi} = \frac{\partial \Phi(\boldsymbol{x}_I)^T}{\partial \xi} \boldsymbol{u} = \left\{ \frac{\partial \Phi(\boldsymbol{x}_I)^T}{\partial \xi} ; \frac{\partial \Psi(\boldsymbol{x}_I)^T}{\partial \xi} \right\} \begin{Bmatrix} \boldsymbol{u} \\ \boldsymbol{z} \end{Bmatrix} \qquad \textbf{2-18}$$

"From equation 2-14 it is possible to write" (Farahani et al. 2015)

$$\left\{\frac{\partial\Phi(\boldsymbol{x}_I)^T}{\partial\xi};\frac{\partial\Psi(\boldsymbol{x}_I)^T}{\partial\xi}\right\}=\frac{\partial\left(\left\{\boldsymbol{r}(\boldsymbol{x}_I)^T;\boldsymbol{p}(\boldsymbol{x}_I)^T\right\}\boldsymbol{G}^{-1}\right)}{\partial\xi} \qquad \textbf{2-19}$$

"Since the moment matrix $\boldsymbol{G}$ does not depend on the variable $\boldsymbol{x}_I$, equation 2-19 can be rewritten as" (Farahani et al. 2015)

$$\left\{\frac{\partial\Phi(\boldsymbol{x}_I)^T}{\partial\xi};\frac{\partial\Psi(\boldsymbol{x}_I)^T}{\partial\xi}\right\}=\left\{\frac{\partial\boldsymbol{r}(\boldsymbol{x}_I)^T}{\partial\xi};\frac{\partial\boldsymbol{p}(\boldsymbol{x}_I)^T}{\partial\xi}\right\}\boldsymbol{G}^{-1} \qquad \textbf{2-20}$$

"The partial derivatives of the MQ-RBF vector $\boldsymbol{r}(\boldsymbol{x}_I)$, with respect to a generic variable ξ, can be obtained for each component $\partial r_i(\boldsymbol{x}_I)/\partial\xi$ with the expression," (Farahani et al. 2015)

$$\frac{\partial r_i(\boldsymbol{x}_I)}{\partial\xi}=2p(\xi_i-\xi_I)(d_{iI}{}^2+c^2)^{p-1} \qquad \textbf{2-21}$$

"The RPI test functions $\Phi(\boldsymbol{x}_I)$ depend uniquely on the distribution of scattered nodes (Belinha 2014). Previous works (Wang and Liu 2002a) (L.M.J.S. Dinis, Natal Jorge, and Belinha 2007) (Belinha 2014) show that RPI test functions possess the Kronecker delta property. Since the obtained RPI test functions have a local compact support it is possible to assemble a well-conditioned and banded stiffness matrix. If a polynomial basis is included, the RPI test functions have reproducing properties and possess the unity partition property (Belinha 2014)" (Farahani et al. 2015).

3. Linear Elastic Solid Mechanics

This chapter covers the detailed setting of the Axisymmetric Discrete Equation System. Also addresses the definition of the Plane Stress Discrete Equation System. Both are efficient approaches to analyze particular geometric objects usually found in many engineering areas. Both reduce enormously the potential number of discrete equations from a classical 3D discrete solid equations analyzes systems to a simple 2D equation system.

3.1. Axisymmetric Discrete Equation System

"In this work, since the complete three-dimensional domain $\Lambda \subset \Re^3$ of the studied circular plates can be obtain by the revolution of a two-dimensional domain section $\Omega \subset \Re^2$ and all the natural and essential boundaries show radial symmetry, it is used the axisymmetric deformation theory. In Figure 1(a) it's shown a general example of a revolution solid. Therefore, it is assumed a body described by the domain $\Omega \subset \Re^2$ and bounded by Γ, where $\Gamma \in \Omega : \Gamma_u \cup \Gamma_t = \Gamma \wedge \Gamma_u \cap \Gamma_t = \varnothing$, being Γ_u the essential boundary and Γ_t the natural boundary" (Farahani et al. 2015).

3.1.1. Variable Fields

"Using the cylindrical coordinate system, Figure 1(a), the complete 3D

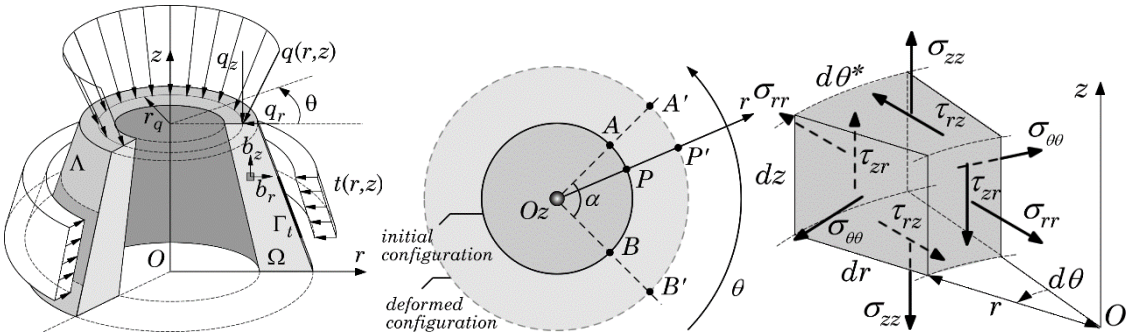

(a) (b) (c)

Figure 1 - (a) Axisymmetric solid. (b) Axisymmetric deformation. (c) Stress components in circular coordinates. Credits: (Farahani et al. 2015)

displacement field can be defined as," (Farahani et al. 2015)

$$\boldsymbol{u}(r,z)=\begin{Bmatrix} u_r(r,z) \\ u_z(r,z) \\ u_\theta(r,z) \end{Bmatrix}. \qquad \textbf{3-1}$$

"The deformation field is determined with, "(Farahani et al. 2015)

$$\varepsilon = \begin{Bmatrix} \varepsilon_{rr} \\ \varepsilon_{zz} \\ \varepsilon_{\theta\theta} \\ \gamma_{rz} \\ \gamma_{z\theta} \\ \gamma_{\theta r} \end{Bmatrix} = \boldsymbol{L}\,\boldsymbol{u} = \begin{bmatrix} \frac{\partial}{\partial r} & 0 & 0 \\ 0 & \frac{\partial}{\partial z} & 0 \\ 0 & 0 & \frac{\partial}{\partial \theta} \\ \frac{\partial}{\partial z} & \frac{\partial}{\partial r} & 0 \\ 0 & \frac{\partial}{\partial \theta} & \frac{\partial}{\partial z} \\ \frac{\partial}{\partial \theta} & 0 & \frac{\partial}{\partial r} \end{bmatrix} \begin{Bmatrix} u_r(r,z) \\ u_z(r,z) \\ u_\theta(r,z) \end{Bmatrix} = \begin{Bmatrix} \frac{\partial u_r}{\partial r} \\ \frac{\partial u_z}{\partial z} \\ \frac{\partial u_\theta}{\partial \theta} \\ \frac{\partial u_r}{\partial z} + \frac{\partial u_z}{\partial r} \\ \frac{\partial u_z}{\partial \theta} + \frac{\partial u_\theta}{\partial z} \\ \frac{\partial u_r}{\partial \theta} + \frac{\partial u_\theta}{\partial r} \end{Bmatrix}. \quad \textbf{3-2}$$

"However, due to the circumferential symmetry of all problems studied in this work, the circumferential coordinate is in fact dependent of the other two coordinates,

$$u_\theta(r,z) = f(u_r, u_z), \quad \textbf{3-3}$$

which is one of the assumptions of the axisymmetric deformation theory. Thus, it is considered that the deformation only occurs in the Orz plane, being the displacement field described by," (Farahani et al. 2015)

$$\boldsymbol{u}(r,z) = \begin{Bmatrix} u_r(r,z) \\ u_z(r,z) \end{Bmatrix}. \quad \textbf{3-4}$$

"Consider Figure 1(b), due to the axisymmetric conditions, the angle α between points AB on an initial configuration is the same has the angle between $A'B'$ for a deformed configuration. Additionally, the arch $A'B'$ is a homothetic arch of initial arch AB, indicating that in the circumferential direction θ there will be only volume changes ($\varepsilon_{\theta\theta} \neq 0$) and no distortions will occur ($\gamma_{z\theta} = 0$ and $\gamma_{\theta r} = 0$)." (Farahani et al. 2015)

"Therefore, the deformation components for the axisymmetric deformation theory are the following," (Farahani et al. 2015)

$$\varepsilon = \boldsymbol{L}\boldsymbol{u} = \begin{Bmatrix} \varepsilon_{rr} \\ \varepsilon_{zz} \\ \varepsilon_{\theta\theta} \\ \gamma_{rz} \end{Bmatrix} = \begin{bmatrix} \frac{\partial}{\partial r} & 0 \\ 0 & \frac{\partial}{\partial z} \\ \frac{1}{r} & 0 \\ \frac{\partial}{\partial z} & \frac{\partial}{\partial r} \end{bmatrix} \begin{Bmatrix} u_r(r,z) \\ u_z(r,z) \end{Bmatrix} = \begin{Bmatrix} \frac{\partial u_r}{\partial r} \\ \frac{\partial u_z}{\partial z} \\ \frac{u_r}{r} \\ \frac{\partial u_r}{\partial z} + \frac{\partial u_z}{\partial r} \end{Bmatrix}. \quad \textbf{3-5}$$

"In order to determine the deformation in the circumferential direction θ, $\varepsilon_{\theta\theta}$ presented in equation 3-5, consider point $P \in A\bar{B}$ represented in Figure 1(b). The deformation of P occurs along the Or axis, leading to point P' and showing a radial displacement: $u_r(r_P, z_P)$. Notice that, due to the axisymmetric assumptions, the displacement field does not depend on the circumferential direction θ: $u_r(r_P, z_P) = u_r(r_A, z_A) = u_r(r_B, z_B)$. Thus, the deformation on the circumferential direction can be obtained with," (Farahani et al. 2015)

$$\varepsilon_{\theta\theta} = \frac{A'\bar{B}' - A\bar{B}}{A\bar{B}} = \frac{\alpha(r + u_r) - \alpha r}{\alpha r} = \frac{u_r}{r}. \quad \textbf{3-6}$$

"The generalized Hooke law permits to correlate the strain field with the stress field,

$$\sigma = \boldsymbol{c}\varepsilon = \begin{Bmatrix} \sigma_{rr} \\ \sigma_{zz} \\ \sigma_{\theta\theta} \\ \tau_{rz} \end{Bmatrix} = \boldsymbol{c} \begin{Bmatrix} \varepsilon_{rr} \\ \varepsilon_{zz} \\ \varepsilon_{\theta\theta} \\ \gamma_{rz} \end{Bmatrix}, \quad \textbf{3-7}$$

being $\boldsymbol{c}$ the material constitutive matrix, defined for the isotropic case as," (Farahani et al. 2015)

$$c = \frac{E}{(1+\upsilon)(1-2\upsilon)} \begin{bmatrix} 1-\upsilon & \upsilon & \upsilon & 0 \\ \upsilon & 1-\upsilon & \upsilon & 0 \\ \upsilon & \upsilon & 1-\upsilon & 0 \\ 0 & 0 & 0 & \frac{1-2\upsilon}{2} \end{bmatrix}. \quad \textbf{3-8}$$

"The Young modulus is represented by E and the Poisson's coefficient by υ" (Farahani et al. 2015).

3.1.2. Weak-form of Galerkin

"The discrete equation system is obtained using the Galerkin weak form. The Lagrangian functional is defined by

$$L = T - U + W_f . \qquad \textbf{3-9}$$

where T is the kinetic energy, U is the strain energy and W_f is the work produced by external forces. Neglecting the dynamic term, the minimization of the Lagrangian functional leads to the Galerkin weak form of the equilibrium equation," (Farahani et al. 2015)

$$\delta L = \int_\Lambda \delta \boldsymbol{\varepsilon}^T \boldsymbol{\sigma}\, d\Lambda - \int_\Lambda \delta \boldsymbol{u}^T \boldsymbol{b}\, d\Lambda - \int_{S_t} \delta \boldsymbol{u}^T \boldsymbol{t}\, dS - \int_{C_q} \delta \boldsymbol{u}^T \boldsymbol{q}\, dC = 0. \qquad \textbf{3-10}$$

"As represented in Figure 1(a), $\boldsymbol{b}$ is the body force, $\bar{\boldsymbol{t}}$ an external force applied along a close surface S_t and $\boldsymbol{q}_i$ are external forces applied along a close curve C_t. Notice that from Figure 1(c), the infinitesimal volume $d\Lambda$ is defined as, $d\Lambda = dr \cdot dz \cdot d\theta^*$, being $d\theta^* = r \cdot \sin(d\theta) \cong r \cdot d\theta$ since $d\theta << 1$, which leads to $d\Lambda = r \cdot d\theta \cdot dr \cdot dz = r \cdot d\theta \cdot d\Omega$. Similarly, it is possible to obtain: $dS = dz \cdot d\theta^* = r \cdot d\theta \cdot dz = r \cdot d\theta \cdot d\Gamma$ and $dC = d\theta^* = r \cdot d\theta$." (Farahani et al. 2015)

"Thus, equation 3-10 can be represented as," (Farahani et al. 2015)

$$\begin{aligned} &\int_\Omega \int_{\theta_i}^{\theta_f} \delta \boldsymbol{\varepsilon}^T \boldsymbol{\sigma}\, r \cdot d\theta \cdot d\Omega = \\ &= \int_\Omega \int_{\theta_i}^{\theta_f} \delta \boldsymbol{u}^T \boldsymbol{b}\, r \cdot d\theta \cdot d\Omega + \int_\Gamma \int_{\theta_i}^{\theta_f} \delta \boldsymbol{u}^T \bar{\boldsymbol{t}}\, r \cdot d\theta \cdot d\Gamma + \int_{\theta_i}^{\theta_f} \delta \boldsymbol{u}^T \boldsymbol{q}\, r \cdot d\theta \end{aligned} . \qquad \textbf{3-11}$$

"The integral along the circumferential direction θ is a defined integral, and since all analysed problems in this work present a full revolution: $\theta_i = 0$ and $\theta_f = 2\pi$,

$$2\pi \int_\Omega r\left(\delta \boldsymbol{\varepsilon}^T \boldsymbol{\sigma}\right) d\Omega = 2\pi \int_\Omega r\left(\delta \boldsymbol{u}^T \boldsymbol{b}\right) d\Omega + 2\pi \int_\Gamma r\left(\delta \boldsymbol{u}^T \bar{\boldsymbol{t}}\right) d\Gamma + 2\pi r\left(\delta \boldsymbol{u}^T \boldsymbol{q}\right). \qquad \textbf{3-12}$$

or" (Farahani et al. 2015)

$$\int_\Omega r\left(\delta \boldsymbol{\varepsilon}^T \boldsymbol{\sigma}\right) d\Omega = \int_\Omega r\left(\delta \boldsymbol{u}^T \boldsymbol{b}\right) d\Omega + \int_\Gamma r\left(\delta \boldsymbol{u}^T \bar{\boldsymbol{t}}\right) d\Gamma + r\left(\delta \boldsymbol{u}^T \boldsymbol{q}\right). \qquad \textbf{3-13}$$

"In the RPIM, the weak form has local support, which means that the discrete system of equations is developed firstly for every influence-domain. Then, the local systems of equations are assembled to form the global system of equations, which is solved afterwards. The RPIM trial function is given by equation 2-17, thus for each degree of freedom it is possible to write,

$$u_r^h(\boldsymbol{x}_I)=\sum_{i=1}^{n}\varphi_i(\boldsymbol{x}_I)u_r(\boldsymbol{x}_i) \quad \text{and} \quad u_z^h(\boldsymbol{x}_I)=\sum_{i=1}^{n}\varphi_i(\boldsymbol{x}_I)u_z(\boldsymbol{x}_i) \qquad \textbf{3-14}$$

where $\varphi_i(\boldsymbol{x}_I)$ is the RPIM interpolation function, $u_r(\boldsymbol{x}_i)$ and $u_z(\boldsymbol{x}_i)$ are the nodal parameters of the i^{th} node belonging to the nodal set defining the influence-domain of interest node $\boldsymbol{x}_I$. Both expressions in equation 3-14 can be combined in one single equation," (Farahani et al. 2015)

$$\boldsymbol{u}^h(\boldsymbol{x}_I)=\begin{Bmatrix}u_r^h(\boldsymbol{x}_I)\\ u_z^h(\boldsymbol{x}_I)\end{Bmatrix}=\sum_{i=1}^{n}\begin{bmatrix}\varphi_i(\boldsymbol{x}_I) & 0\\ 0 & \varphi_i(\boldsymbol{x}_I)\end{bmatrix}\begin{Bmatrix}u(\boldsymbol{x}_i)\\ v(\boldsymbol{x}_i)\end{Bmatrix}=\sum_{i=1}^{n}\boldsymbol{H}_i(\boldsymbol{x}_I)\boldsymbol{u}(\boldsymbol{x}_i). \qquad \textbf{3-15}$$

"Consequently, using equation 3-5 and equation 3-14, it is possible to develop the strain vector to the following expression,

$$\boldsymbol{\varepsilon}(\boldsymbol{x}_I)=\boldsymbol{L}\,\boldsymbol{u}^h(\boldsymbol{x}_I)=\boldsymbol{L}\sum_{i=1}^{n}\boldsymbol{H}_i(\boldsymbol{x}_I)\boldsymbol{u}(\boldsymbol{x}_i)=$$

$$=\sum_{i=1}^{n}\boldsymbol{B}_i(\boldsymbol{x}_I)\boldsymbol{u}(\boldsymbol{x}_i)=\sum_{i=1}^{n}\begin{bmatrix}\dfrac{\partial\varphi_i(\boldsymbol{x}_I)}{\partial r} & 0\\ 0 & \dfrac{\partial\varphi_i(\boldsymbol{x}_I)}{\partial z}\\ \dfrac{\varphi_i(\boldsymbol{x}_I)}{r} & 0\\ \dfrac{\partial\varphi_i(\boldsymbol{x}_I)}{\partial z} & \dfrac{\partial\varphi_i(\boldsymbol{x}_I)}{\partial r}\end{bmatrix}\begin{Bmatrix}u_r(\boldsymbol{x}_i)\\ u_z(\boldsymbol{x}_i)\end{Bmatrix}, \qquad \textbf{3-16}$$

being $\boldsymbol{B}=\boldsymbol{LH}$ the deformation matrix. Using the relation between the stress state and the strain state in equation 3-7, it is possible to obtain for an interest point $\boldsymbol{x}_I$: $\boldsymbol{\sigma}(\boldsymbol{x}_I)=\boldsymbol{c}\,\boldsymbol{\varepsilon}(\boldsymbol{x}_I)$. Substituting the strain vector $\boldsymbol{\varepsilon}(\boldsymbol{x}_I)$ and the stress vector $\boldsymbol{\sigma}(\boldsymbol{x}_I)$ in the first term of equation 3-13 and the approximation function on equation 3-15 in the other terms, it is possible to rewrite equation 3-13 for an interest point $\boldsymbol{x}_I$," (Farahani et al. 2015)

$$\delta \boldsymbol{u}^T \underbrace{\int_\Omega r_I \, \boldsymbol{B}^T \boldsymbol{c} \boldsymbol{B} \, d\Omega}_{\boldsymbol{K}} \boldsymbol{u} = \delta \boldsymbol{u}^T \underbrace{\int_\Omega r_I \, \boldsymbol{H}^T \begin{Bmatrix} b_r \\ b_z \end{Bmatrix} d\Omega}_{\boldsymbol{f}_b} + \delta \boldsymbol{u}^T \underbrace{\int_{\Gamma_t} r_I \boldsymbol{H}^T \begin{Bmatrix} t_r \\ t_z \end{Bmatrix} d\Gamma_t}_{\boldsymbol{f}_t} + \delta \boldsymbol{u}^T \underbrace{r_I \begin{Bmatrix} q_r \\ q_z \end{Bmatrix}}_{\boldsymbol{f}_q} \quad \textbf{3-17}$$

"In the end, after assembling the stiffness matrices $\boldsymbol{K}_I$ obtained for each interest point $\boldsymbol{x}_I$, equation 3-17 can be represented as the following linear system of equations," (Farahani et al. 2015)

$$\delta \boldsymbol{u}^T \left[\boldsymbol{K} \boldsymbol{u} - \boldsymbol{f}_b - \boldsymbol{f}_t - \boldsymbol{f}_q \right] = 0 \Rightarrow \boldsymbol{K} \boldsymbol{u} = \boldsymbol{f}_b + \boldsymbol{f}_t + \boldsymbol{f}_q \,. \quad \textbf{3-18}$$

"Since the RPI test functions possess the delta Kronecker property, the essential boundary conditions are directly imposed in the global stiffness matrix, $\boldsymbol{K}$ " (Farahani et al. 2015).

3.2. Plane Stress Discrete Equation System

When in a 3D analysis of any solid prism we find that the variables are comfortably independent from one of the Cartesian axis (let's say z axis) one can reduce the problem to a 2D plane strain or plane stress. Plane strain means the strains out of the x-y plane are negligible and hence the solid prism is relatively thicker in the z direction. Plane Stress is considered when the stresses out of the plane x-y are negligible and hence the solid prism is thinner in the z direction. Also besides that basic lines of definition, both plane strain or plane stress have negligible strain or stress in z direction (G. Liu and Karamanlidis 2003).

We can reduce the 3D case with 6 independent strain components to a simpler case of just 3 variables. Hence the deformation field is determined with,

$$\boldsymbol{\varepsilon} = \begin{Bmatrix} \boldsymbol{\varepsilon_{xx}} \\ \boldsymbol{\varepsilon_{xx}} \\ \boldsymbol{\varepsilon_{xx}} \end{Bmatrix} = \begin{Bmatrix} \boldsymbol{\frac{du}{dx}} \\ \boldsymbol{\frac{dv}{dy}} \\ \boldsymbol{\frac{du}{dy} + \frac{dv}{dx}} \end{Bmatrix}. \qquad \textbf{3-19}$$

Where *u* is the displacement in x direction and *v* in y direction (G. Liu and Karamanlidis 2003).

The arrangement of the displacement field is suggested to be like follows (G. Liu and Karamanlidis 2003),

$$\boldsymbol{u} = \begin{Bmatrix} \boldsymbol{u} \\ \boldsymbol{v} \end{Bmatrix} \qquad \textbf{3-20}$$

3.2.1. Constitutive equations

We obtain the stresses through Hook's law in matrix formulation:

$$\boldsymbol{\sigma} = \mathbf{c}\boldsymbol{\varepsilon}. \qquad \textbf{3-21}$$

Where **c** is the constitutive matrix of the material. Their constant values are commonly obtain directly from experimental data when in elastic regime. For the isotropic case we have the following matrix for *plane stress* (G. Liu and Karamanlidis 2003),

$$\mathbf{c} = \frac{\mathbf{E}}{\mathbf{1}-\boldsymbol{\nu}^{\mathbf{2}}}\begin{bmatrix} \mathbf{1} & \boldsymbol{\nu} & \mathbf{0} \\ \boldsymbol{\nu} & \mathbf{1} & \mathbf{0} \\ \mathbf{0} & \mathbf{0} & \frac{\mathbf{1}-\boldsymbol{\nu}}{\mathbf{2}} \end{bmatrix}. \qquad \textbf{3-22}$$

4. Nonlinear Mechanics: Damage

Damage is a continuum mechanics numerical convenient concept to numerically reproduce what can occur in some materials related to change in stiffness, crack propagation and failure. Damage it is not unique in predict failure but it's one of the most important state of the art techniques available today. Damage also is found in many perspectives of implementation from diverse authors. For example Nonlocal and Local damage (Faria, Oliver, and Cervera 1998) (Cervera, Oliver, and Manzoli 1996).

The present work intend to follow the implementation of damage as presented by Cervera et al., (Faria, Oliver, and Cervera 1998) (Cervera, Oliver, and Manzoli 1996), with traction damage law called by some authors, (Polanco-Loria and S¢rensen 1995), of Oliver's law.

It was recorded in some material experiments like concrete, that after reach some load value to a specimen, when it was unloaded the 'returning' path suggesting that the elasticity slope (Young modulus, *E*) had decreased. Also the material kept that 'new' *E*, even when loaded and unloaded in elastic regime. Especially in materials like concrete or even soil it seem to exists the same softening phenomenon (decrease of *E*) but with different rates or magnitudes of evolution patterns. Other much older concept in computational continuum mechanics is plasticity, but some of the experiments showed high softening and negligible plasticity like behavior (Faria, Oliver, and Cervera 1998) (Cervera, Oliver, and Manzoli 1996).

So damage has been filling a gap to more widely and accurately predict different material properties evolutions (Faria, Oliver, and Cervera 1998) (Cervera, Oliver, and Manzoli 1996).

Some light can be brought in to this subject, particularly with the traction damage phenomenon. It is possible to imagine some prismatic objects subjected to tensile loads till some holes start to appear, similar to *cheese* holes. Having this picture in mind the concept is this:

(1) Before the holes appear, elastic regime;

(2) After holes appear, nonlinear regime.

Case (1) is trivial and case (2) led to the need of the variable damage, *D.* This variable usually has values in interval [0, 1], with no units. This is simple to understand in a mathematical point of view especially for a 1D uniaxial tensile test. The relation of damage with the constitutive variable, *E*, is straightforward (Faria, Oliver, and Cervera 1998) (Cervera, Oliver, and Manzoli 1996):

$$\boldsymbol{\sigma} = (\mathbf{1} - \boldsymbol{d})\boldsymbol{E}\boldsymbol{\varepsilon} \qquad \textbf{4-1}$$

Case (1) would imply *d* = 0, or no softening of *E.* Case (2) would be *d* = one value in the interval]0, 1], meaning softening has occurred for that strain state. Also it is assumed in damage theory that strain state of a damaged material is equal to the strain state of that material if no damage had occurred in it. So a routine of damage directly corrects the stresses like the simple case of equation 4-1. This has, after all, a subtle but interesting detail. One isolated (without iterative convergence process) incremental step of imposed displacement will do that, meaning 'after damage', strains are the same of any trial elastic step. But when the iterative process is activated, the strains will ultimately be targets of the successive residual vectors that are applied in any trivial iterative scheme. Anyway this particularity doesn't invalidate the truthiness of that first assumption of the equivalence of strains within any direct computation (Faria, Oliver, and Cervera 1998) (Cervera, Oliver, and Manzoli 1996).

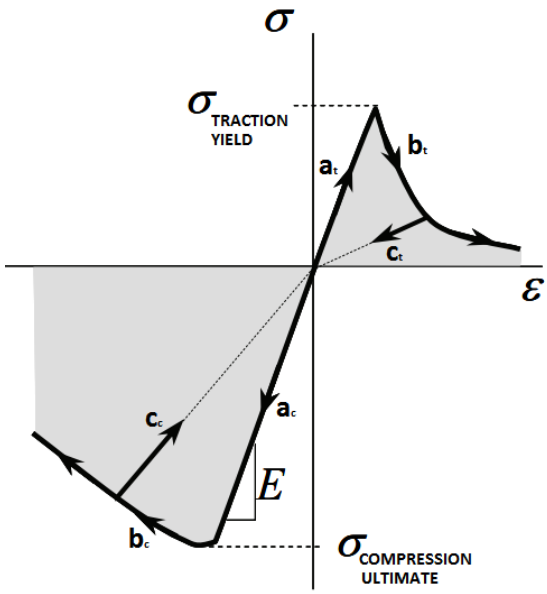

Figure 2 – Traction softening load (b_t) and traction 'softened' unload (c_t). Compression softening load (b_c), and traction 'softened' unload (c_c).

Figure 2 show a 1D softening sequence both for traction and for compression. In concrete traction damage, σ_0^+ (yield stress) is coincident with σ_U^+ (ultimate stress). This is due to the brittle nature of concrete traction damage law. But in concrete compression damage, σ_0^- (yield stress) has an absolute value noticeable lower than σ_c^- (ultimate stress). This 1D analogy it is not just only a useful tool to faster understanding of the damage effect in constitutive material properties. This 1D, or scalar, space can be recursive even if we are in 2D or 3D numerical simulation. Isotropic damage as the one of this work is independent of local geometry orientation and is also scalar. Meaning that, despite of stress vectors can have one (1D), three (2D) or six (3D) independent components, each gauss stress vector will be affected by a single scalar damage variable (independent of any Cartesian axis orientation). But for the particular case of concrete constitutive damage model exists a traction evolution law different from an also present compression law. This leads to a necessary split of the scalar damage: in compression damage, d^-, and in traction damage, d^+. Consequently we observe a split of stress vector

in σ^- and σ^+, respectively (Faria, Oliver, and Cervera 1998) (Cervera, Oliver, and Manzoli 1996).

4.1. Multidimensional Rate-Independent Model

It was suggested, (Cervera, Oliver, and Manzoli 1996) (Faria, Oliver, and Cervera 1998), that by Continuum Damage Mechanics Theory (CDMT) effective stress tensor (second order), $\overline{\boldsymbol{\sigma}}$, is similar to any elastic trial stress tensor:

$$\overline{\boldsymbol{\sigma}} = \boldsymbol{D_0}\boldsymbol{:}\boldsymbol{\varepsilon} \qquad \textbf{4-2}$$

Where $\boldsymbol{D_0}$, is the constitutive elastic fourth order tensor and $\boldsymbol{\varepsilon}$ is the strain second order tensor and '$\boldsymbol{:}$' denotes tensor double contraction operation. This equivalence is possible because strain of a damaged state is equivalent (or equal) to an undamaged state (elastic trial). Besides the fact of using isotropic damage model, concrete properties demand a different consideration either for compression or traction strains or stresses. So the split for stresses in the present work was made as follows (Faria, Oliver, and Cervera 1998) (Cervera, Oliver, and Manzoli 1996):

$$\overline{\boldsymbol{\sigma}}^{+}_{\boldsymbol{normal}} = \; < \overline{\boldsymbol{\sigma}}_{\boldsymbol{normal}} > \; = \begin{bmatrix} \boldsymbol{\sigma_1^+} & \mathbf{0} & \mathbf{0} \\ \mathbf{0} & \boldsymbol{\sigma_2^+} & \mathbf{0} \\ \mathbf{0} & \mathbf{0} & \boldsymbol{\sigma_3^+} \end{bmatrix}. \qquad \textbf{4-3}$$

$$\overline{\boldsymbol{\sigma}}^{-}_{\boldsymbol{normal}} = \; > \overline{\boldsymbol{\sigma}}_{\boldsymbol{normal}} < \; = \begin{bmatrix} \boldsymbol{\sigma_1^-} & \mathbf{0} & \mathbf{0} \\ \mathbf{0} & \boldsymbol{\sigma_2^-} & \mathbf{0} \\ \mathbf{0} & \mathbf{0} & \boldsymbol{\sigma_3^-} \end{bmatrix}. \qquad \textbf{4-4}$$

Where for equation 4-3 only positive valued principal stresses go to the respective matrix (second order tensor) diagonal entries and for equation 4-4 only negative valued principal stresses go to the respective matrix (second order tensor) diagonal entries, or zeros otherwise. Split can be made by any mathematical suitable means. After that, one can 'rotate' back those normal stresses in trial Cartesian stress tensors (or trial Cauchy

stress tensors, $\bar{\boldsymbol{\sigma}}^{+}$and $\bar{\boldsymbol{\sigma}}^{-}$**).** After that, the split of Cauchy stress tensor, $\boldsymbol{\sigma}$, can also be made explicitly (Faria, Oliver, and Cervera 1998) (Cervera, Oliver, and Manzoli 1996):

$$\boldsymbol{\sigma} = (\mathbf{1} - \boldsymbol{d}^{+})\bar{\boldsymbol{\sigma}}^{+} + (\mathbf{1} - \boldsymbol{d}^{-})\bar{\boldsymbol{\sigma}}^{-} \qquad \textbf{4-5}$$

Where

$$\mathbf{0} \leq \boldsymbol{d}^{+} \leq \mathbf{1}\ \boldsymbol{and}\ \mathbf{0} \leq \boldsymbol{d}^{-} \leq \mathbf{1} \qquad \textbf{4-6}$$

Here d^{+} and d^{-} are respectively the traction and compression scalar damage variables. Depending on the specific material of any study this variables will have particular evolution laws (Faria, Oliver, and Cervera 1998) (Cervera, Oliver, and Manzoli 1996).

By some convenience, (Cervera, Oliver, and Manzoli 1996) (Faria, Oliver, and Cervera 1998), a *norm* (scalar) mathematical space was used instead of direct use of the compression tensor strains, $\boldsymbol{\varepsilon}^{-}$, and stresses, $\boldsymbol{\sigma}^{-}$, or traction tensor strains, $\boldsymbol{\varepsilon}^{+}$, and stresses, $\boldsymbol{\sigma}^{+}$. The authors of that work suggested the following correspondence, defining traction norm, τ^{+}:

$$\boldsymbol{\tau}^{+} = \sqrt{\bar{\boldsymbol{\sigma}}^{+} : \boldsymbol{D}_{\mathbf{0}}^{-\mathbf{1}} : \bar{\boldsymbol{\sigma}}^{+}}. \qquad \textbf{4-7}$$

Where $\bar{\boldsymbol{\sigma}}^{+}$ is the stress tensor and the units of τ^{+} are $Pa^{1/2}$ and also are the units for their suggested compression norm, τ^{-} that is defined by equation 4-8:

$$\boldsymbol{\tau}^{-} = \sqrt{\sqrt{\mathbf{3}}(\boldsymbol{K}\bar{\boldsymbol{\sigma}}_{\boldsymbol{oct}}^{-} + \bar{\boldsymbol{\tau}}_{\boldsymbol{oct}}^{-})}. \qquad \textbf{4-8}$$

Where K is a material constant with typical values of K = 0.171, $\bar{\sigma}_{oct}^{-}$ is the octahedral normal stress and $\bar{\tau}_{oct}^{-}$ is the octahedral shear stress. This simplification allows distinct three or two dimensional stress states to be suitable of comparison (Faria, Oliver, and Cervera 1998) (Cervera, Oliver, and Manzoli 1996).

We reach now to the traction and compression scalar damage split criteria, g^{+} and g^{-} (Faria, Oliver, and Cervera 1998) (Cervera, Oliver, and Manzoli 1996):

$$g^{+}(\bar{\tau}^{+}, r^{+}) = \bar{\tau}^{+} - r^{+} \leq 0 \qquad \textbf{4-9}$$

$$g^{-}(\bar{\tau}^{-}, r^{-}) = \bar{\tau}^{-} - r^{-} \leq 0 \qquad \textbf{4-10}$$

The variables r^{+} and r^{-} are the most recent updated thresholds with $Pa^{1/2}$ units. Initially those two variables can be easily be defined through the yielding values of the material properties (Faria, Oliver, and Cervera 1998) (Cervera, Oliver, and Manzoli 1996):

$$r_0^{+} = \sqrt{f_0^{+} \frac{1}{E} f_0^{+}} = \frac{f_0^{+}}{\sqrt{E}} \qquad \textbf{4-11}$$

$$r_0^{-} = \sqrt{\frac{\sqrt{3}}{3}(K - \sqrt{2}) f_0^{-}} \qquad \textbf{4-12}$$

Where E is the Young modulus, f_0^{+} is the tensile yield stress and f_0^{-} is the compression yield stress (Faria, Oliver, and Cervera 1998) (Cervera, Oliver, and Manzoli 1996).

Once the incremental or iterative schemes proceed, those equations cannot be used as the means to compute the updated thresholds. The adopted, (Cervera, Oliver, and Manzoli 1996) (Faria, Oliver, and Cervera 1998), simple way of compute those variables needs to be as follows:

$$r^{+} = \max(r_0^{+}, \max(\tau^{+})) \qquad \textbf{4-13}$$

$$r^{-} = \max(r_0^{-}, \max(\tau^{-})) \qquad \textbf{4-14}$$

And first, the traction damage evolution law can be computed respectively using some of those convenient previously defined variables (Faria, Oliver, and Cervera 1998) (Cervera, Oliver, and Manzoli 1996):

$$d^{+} = 1 - \frac{r_0^{+}}{r^{+}} e^{A^{+}\left(1 - \frac{r^{+}}{r_0^{+}}\right)} \qquad \textbf{4-15}$$

Where A^{+}, is a traction damage parameter that can be computed as in equation 4-16:

$$A^{+} = \frac{f_0^{+2} l_{CH}}{E G_f^{+} - \frac{1}{2} f_0^{+2} l_{CH}} \qquad \textbf{4-16}$$

Where G_f^{+} is the fracture energy released per unit length and l_{CH}, is the usually called mesh *characteristic length* and it corresponds (in *Finite Element Method, FEM*) to the length (1D) of the element, the square root of the area (2D) of the element or to the cube root (3D) of the volume of the element. The crack band width, l_{crack}, which comes from experimental data (Polanco-Loria and S¢rensen 1995) is also commonly called by 'characteristic length' and can be defined as:

$$l_{crack} = \frac{G_f^{+}}{g_f^{+}} \qquad \textbf{4-17}$$

Where g_f^{+} is the total specific dissipated energy (the area under the σ^{+}-ε^{+} curve), or equivalently it is the fracture energy release per unit volume. In the present work however some preliminary attempts failed to implement this fully ideal objectivity of the mesh local damage model. For example, without positive outcome, it was tried the square root of the gauss function area, the square root of the total integration cell and the average nodal spacing surrounding a gauss point as candidates for a reasonable characteristic length, all without success. But it was suggested in other work, (Polanco-Loria and S¢rensen 1995), a 'fixed' ('mesh independent') characteristic length, l_{CH}, (even for local damage) but keeping everything else already set:

$$l_{CH} = \frac{2EG_f^+}{f_0^{+2}} = \frac{2G_f^+}{E\varepsilon_0^{+2}} \qquad \text{4-18}$$

This means that in this present work, using a meshless method, the RPIM, is arbitrarily assumed $l_{CH} = l_{crack}$. This approach is usually called in literature of approach with lack of mesh objectivity, but still is a local damage model. One especial attention in this work was to maintain the most regular spaced nodes possible in mutual damaged areas. Future work should search for a suitable relation between a mesh dependent *characteristic length,* $l_{CH,}$ and any relevant mesh parameter in RPIM routines. Still for traction an example from another work, (Cervera, Oliver, and Manzoli 1996), can show a typical concrete stress and damage traction load-unload curves, as plotted in Figure 3.

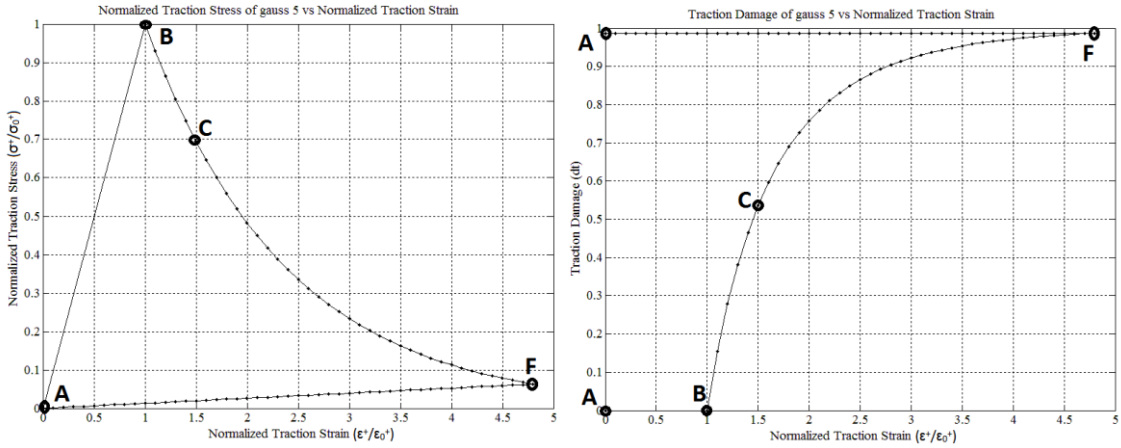

Figure 3 – Example of typical load-unload stress and damage traction curves. Simulation input data from a Cervera et al. example, (Cervera, Oliver, and Manzoli 1996).

And now, the compression damage evolution law can be computed respectively using some of those convenient previously defined variables (Cervera, Oliver, and Manzoli 1996):

$$d^- = 1 - \frac{r_0^-}{r^-}(1 - A^-) - A^- e^{B^-\left(1 - \frac{r^-}{r_0^-}\right)} \qquad \textbf{4-19}$$

The parameters A^- and B^- can be defined either by imposing at least 2 points from an experimental test evolution curve. Finally, for compression, a reproduced example from the other work data, (Cervera, Oliver, and Manzoli 1996), can show a typical concrete stress and damage traction load-unload curves as plotted in Figure 4.

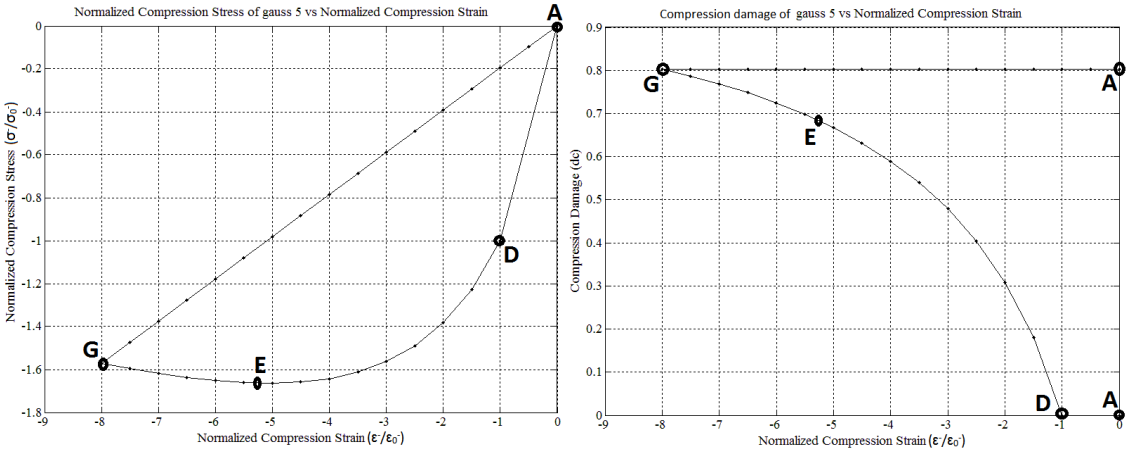

Figure 4 - Example of typical load-unload stress and damage compression curves. Simulation input data from a Cervera et al. example, (Cervera, Oliver, and Manzoli 1996).

The Figure 5 details the algorithm to evaluate the 'final' stress tensor. This is made for each increment, or more specifically, for each iteration. This 'final' stress tensor is used to compute the internal force vector.

Input variables: $r_n^+, r_n^-, \boldsymbol{\varepsilon_{n+1}}$

Output variables: $r_{n+1}^+, r_{n+1}^-, \boldsymbol{\sigma_{n+1}}$

(1) Evaluate trial stresses $\overline{\boldsymbol{\sigma}}_{\boldsymbol{n+1}} = \boldsymbol{D_0 : \varepsilon_{n+1}}$

(2) Split $\overline{\boldsymbol{\sigma}}_{\boldsymbol{n+1}}$ into $\overline{\boldsymbol{\sigma}}_{\boldsymbol{n+1}}^+$ and $\overline{\boldsymbol{\sigma}}_{\boldsymbol{n+1}}^-$ (Eq. 4-3 and Eq. 4-4)

(3) Compute equivalent stress norms τ_{n+1}^+ and τ_{n+1}^- (Eq. 4-7 and Eq. 4-8)

(4) Evaluate damage variables:

d_{n+1}^+ (Eq. 4-15)

d_{n+1}^- (Eq. 4-19)

(5) Compute **FINAL** stress tensor

$$\boldsymbol{\sigma_{n+1}} = (1 - d_{n+1}^+)\overline{\boldsymbol{\sigma}}_{\boldsymbol{n+1}}^+ + (1 - d_{n+1}^-)\overline{\boldsymbol{\sigma}}_{\boldsymbol{n+1}}^-$$

Figure 5 – Algorithm for the evaluation of stresses in each gauss point (Cervera, Oliver, and Manzoli 1996)

5. Numerical Examples

"In this section, first the RPIM is calibrated and validated for the axisymmetric deformation theory using the weak formulation of Galerkin. Afterwards, one example of circular plate, one example of concrete beam and one example of reinforced concrete beam are analysed. The first examples are compared with the FEM solution obtained with the commercial FEM software ANSYS and one analytical solution. In the FEM analysis it was used the PLANE182 element, which is a linear four-node axisymmetric element. The later examples are compared mainly with experimental data." (Farahani et al. 2015)

5.1. Circular Plate under Uniform Distributed Load

"In this work was choose to present the transversal centre displacement of the circular plate in full magnitude, $u_z(r=0)$ and the normalized value, $\bar{u}_z(r=0)$ which can be determined with:

$$\bar{u}_z(0) = 100 \times u_z(0) \times \left(\frac{E\ H^3}{R^4\ q} \right). \qquad \textbf{5-1}$$

where q is the magnitude of external force applied on the circular plate and E the material elasticity modulus. The scalars R and H represent the radius and the thickness of the plate respectively." (Farahani et al. 2015)

"Additionally, the first order local error on the centre of the plate is presented in convenient graphics,

$$error = \frac{u_z(r=0)^{RPIM} - u_z(r=0)^{exact}}{u_z(r=0)^{exact}}, \qquad \textbf{5-2}$$

being $u_z(r=0)^{RPIM}$ the solution obtained with the meshless method and $u_z(r=0)^{exact}$ the solution obtained with the considered exact solution." (Farahani et al. 2015)

"Regarding the material properties, in the axisymmetric example are considered: Elasticity modulus $E = 10^6\, Pa$ and Poisson's coefficient $\upsilon = 0.3$." (Farahani et al. 2015)

Table 1 - Material properties for axisymmetric analysis

Material	Young modulus, E [MPa]	*Poisson ratio, v*
General Material	1.0	0.3

"In this section it is studied a circular plate under a uniform distributed load (UDL) with magnitude: $q = 100N/m^2$. Two distinct boundary conditions are studied, which include simply supported (SSSS) and clamped (CCCC) contours. The analytical solution of the circular plate for the displacement of the circular SSSS plate under an UDL is obtained from the following expression (Timoshenko and Woinowsky-Krieger, n.d.)," (Farahani et al. 2015)

$$u_z(r) = \frac{q\left(R^2 - r^2\right)\left[\left(\frac{5+\upsilon}{1+\upsilon}\right)R^2 - r^2\right]}{\frac{64\,E\,H^3}{12\left(1-\upsilon^2\right)}}. \qquad \textbf{5-3}$$

"The analytical solution of the circular CCCC plate submitted to a UDL is obtained with,

$$u_z(r) = \frac{q\left(R^2 - r^2\right)^2}{\frac{64\,E\,H^3}{12\left(1-\upsilon^2\right)}}. \qquad \textbf{5-4}$$

where r is defined as the distance between the interest point P and the centre of the plate, Figure 6." (Farahani et al. 2015)

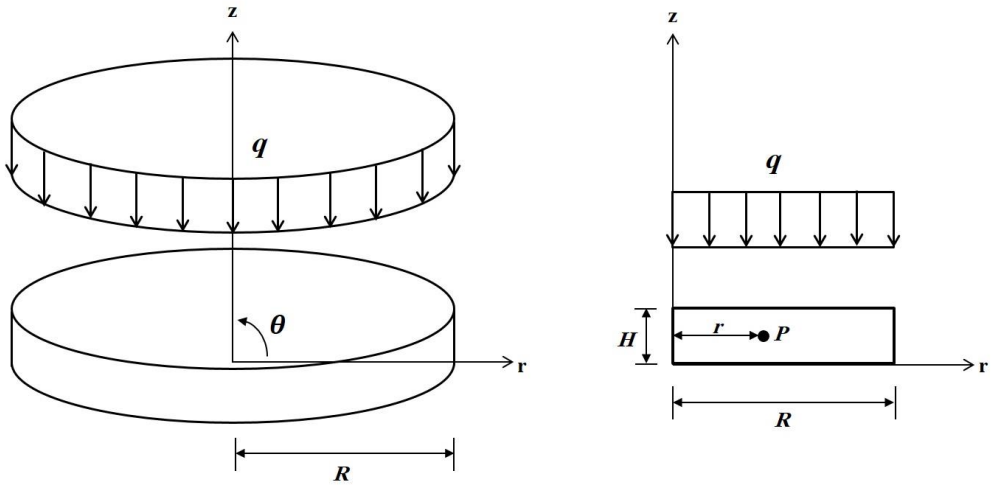

Figure 6 – Circular plate under uniform distributed load. Credits: (Farahani et al. 2015)

5.1.1. Convergence Study

"In this subsection the convergence rate of the RPIM is studied. Consider the two-dimensional domain presented in Figure 6. In this study it is considered the following dimensions: $R = 20m$ and $H = 1m$. The problem domain is discretized in a regular mesh of $n_r \times n_z$ nodes, being n_r the number of nodes along the direction r and n_z the number of nodes on direction z. The problem was analysed using the RPIM and the FEM. Both numerical solutions are compared with the analytical exact solution for the SSSS circular plate, equation 5-3, and for the CCCC circular plate, equation 5-4." (Farahani et al. 2015)

"The results regarding the convergence study are shown in Figure 7 and Figure 8 respectively for the SSSS and the CCCC cases. The results show that the final converged values of the RPIM solutions and the FEM solutions are very close to each other, Figure 7 and Figure 8. Additionally, it is visible that using more than 123 nodes permits to obtain errors below 1%." (Farahani et al. 2015)

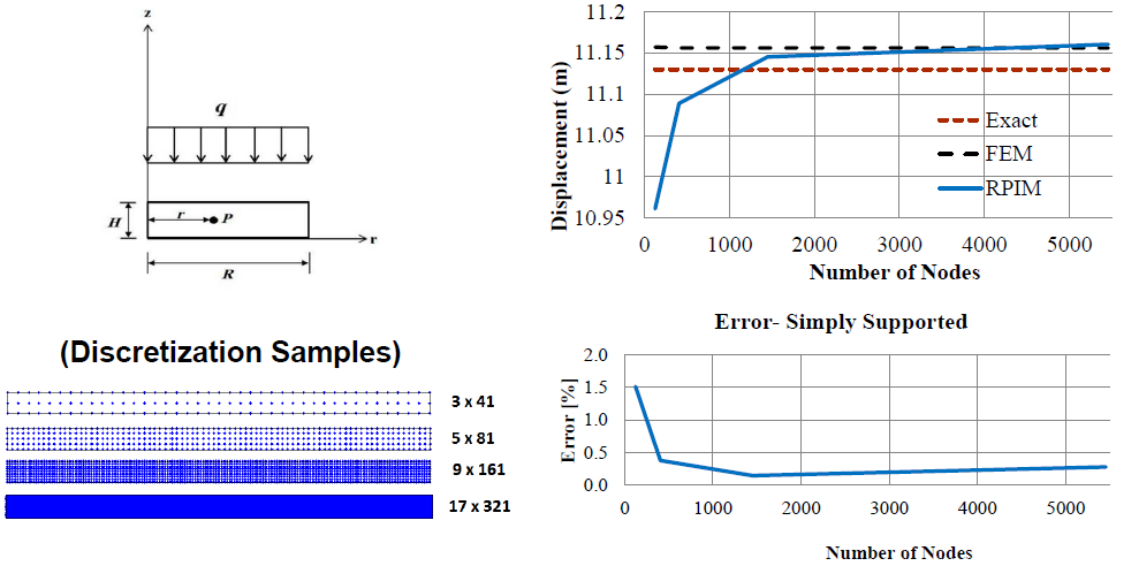

Figure 7 - Transversal displacement (CENTER) values obtained from Exact, RPIM and FEM methods regarding of number of nodes *(SIMPLY SUPPORTED). Error of RPIM compared to Exact. . Credits:* (Farahani et al. 2015)

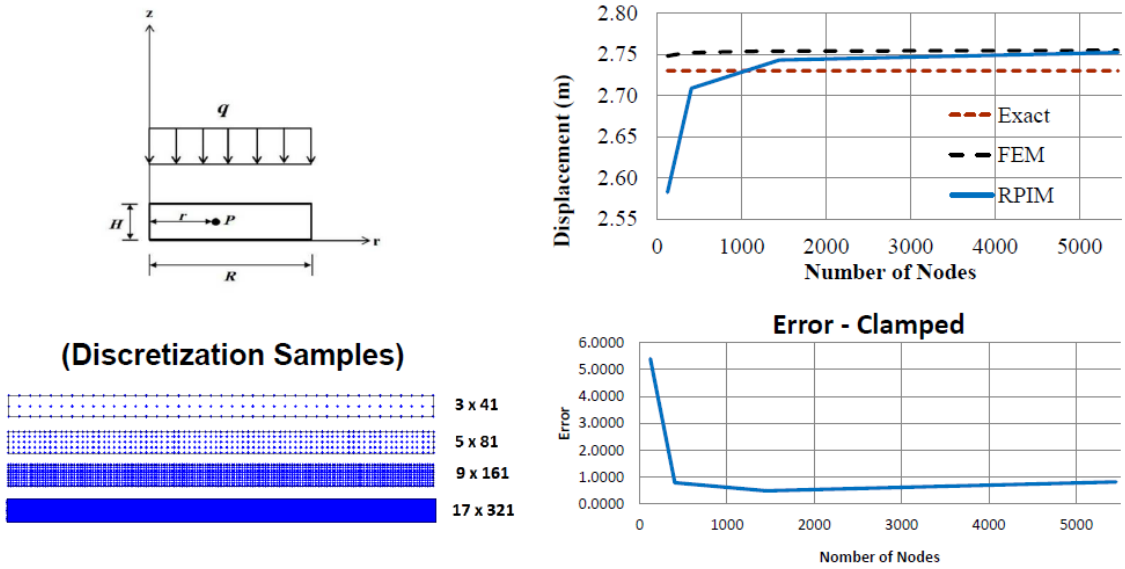

Figure 8 - Transversal displacement (CENTER) values obtained from Exact, RPIM and FEM methods regarding of number of nodes *(CLAMPED). Error of RPIM compared to Exact. . Credits:* (Farahani et al. 2015)

5.1.2. Numerical Integration Scheme

"In order to determine the optimal number of integration points inside every integration cell, it is required to perform a transversal study on the several quadrature schemes of Gaussian points inside the integration cell." (Farahani et al. 2015)

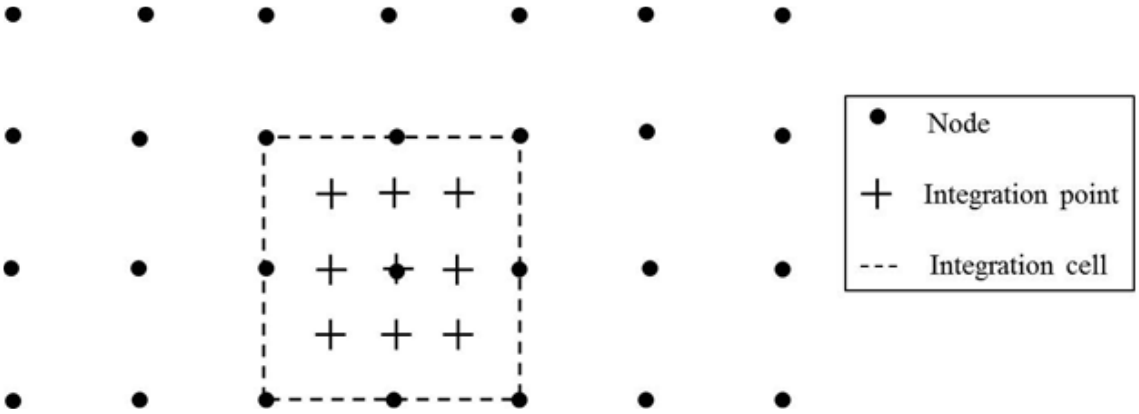

Figure 9 - Example of an integration cell with 3x3 integration points inside. Credits: (Farahani et al. 2015)

"Consider Figure 9, in which a general example of an integration cell is presented. Inside the integration cell are inserted 3×3 integration points respecting the Gauss-Legendre quadrature scheme. In this study all the integration cells respect the geometric disposition shown in Figure 9, i.e. all integration cells contain 9 nodes and $n_Q \times n_Q$ integration points respecting the Gauss-Legendre quadrature scheme. Aiming to determine the optimal number of integration points inside each integration cell, the value n_Q was varied between 2 and 10. All the material, geometrical and loading conditions considered in subsection 5.1.1 are assumed. The results for the SSSS and the CCCC cases are shown respectively in Figure 10." (Farahani et al. 2015)

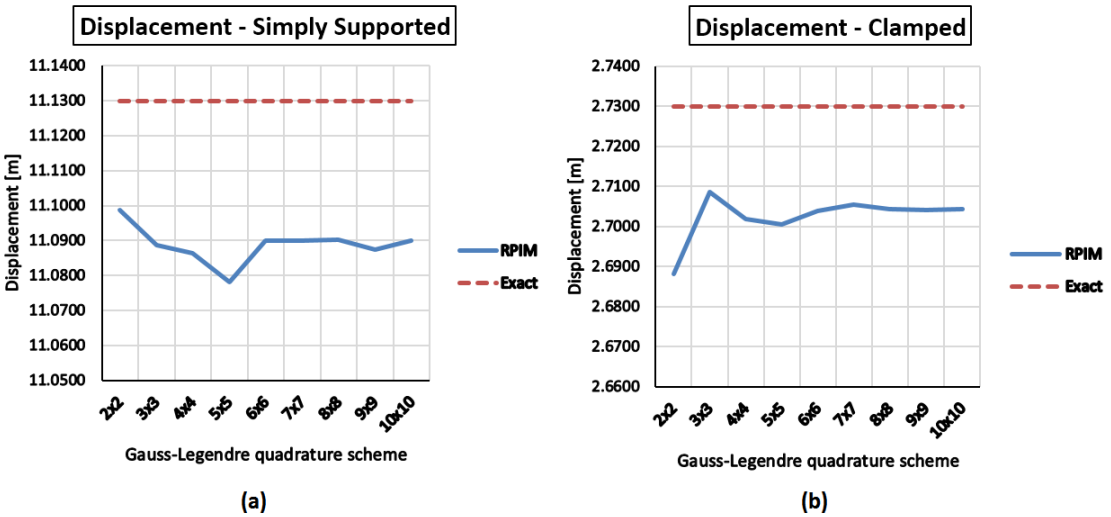

Figure 10 - Transversal displacement values obtained for each integration scheme for the exact solution, RPIM method respectively for the SSSS case (a) and the CCCC case (b). Credits: (Farahani et al. 2015)

"The values on the Figure 10 indicate that the solution starts to stabilize to integration schemes using $n_Q > 5$. However, the increase of n_Q increases the computational cost of the RPIM analysis. Thus, in this work, in all further examples it is used 3×3 integration points inside each integration cell, since with this integration scheme it is possible to obtain solutions showing acceptable errors (below 0.8%) without increasing significantly the computational cost of the analysis." (Farahani et al. 2015)

5.1.3. Influence Domain

"This subsection purposes to determine the optimal number of nodes inside the influence-domains. Thus, first it is assumed a circular plate showing the same geometrical properties of previous subsections. The material properties and the external load conditions are coincident as well. The problem domain is then discretized in a regular mesh of 81x5 nodes and an integration background mesh is constructed, as described in subsection 5.1.2, Figure 9. Afterwards each integration point $\boldsymbol{x}_I$ searches for the closest N_I nodes. These N_I nodes: $N_I = \{n_1, n_2, \ldots, n_{N_I}\}$, form the influence-domain of interest point $\boldsymbol{x}_I$. In order to obtain the optimal value for N_I, the described example was studied considering 34 integer values for $N_I = \{8, 9, \ldots, 40, 41\}$." (Farahani et al. 2015)

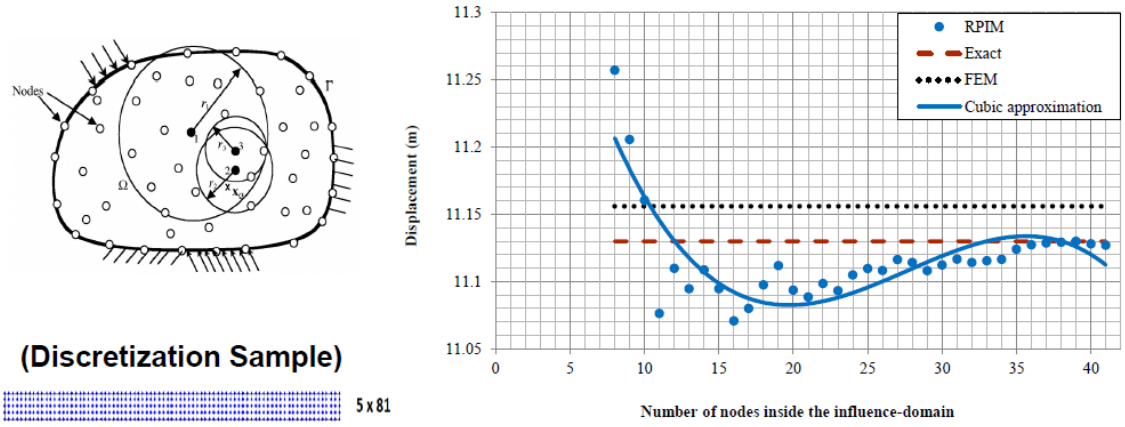

Figure 11 - Transversal displacement values obtained from RPIM, exact and FEM regarding the number of nodes inside the influence-domain for SSSS case. Credits: (Farahani et al. 2015)

"The transversal centre displacements of each study is presented in Figure 11 for the SSSS circular plate and in Figure 12 for the CCCC circular plate. For comparison purposes it is presented also the FEM solution and the analytical solution (which are constant since both do not depend on N_I)." (Farahani et al. 2015)

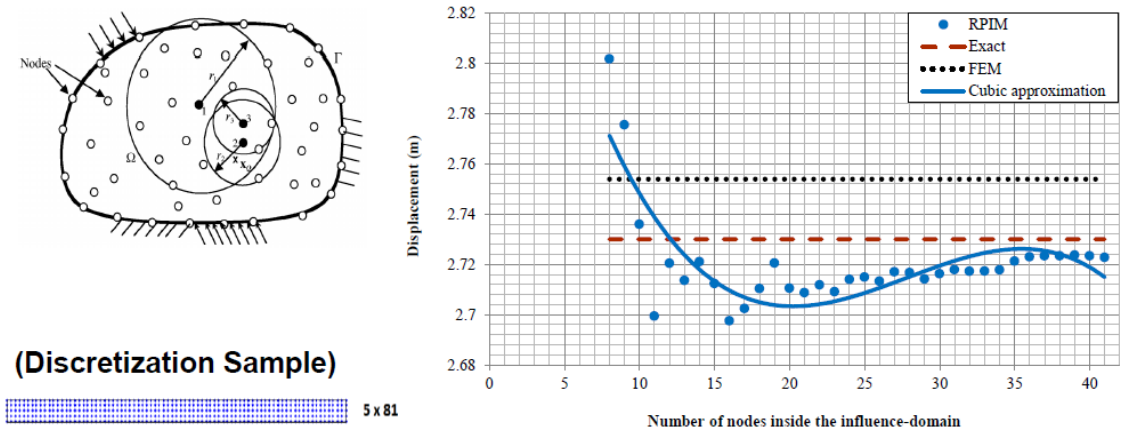

Figure 12 - Transversal displacement values obtained from RPIM, exact and FEM regarding the number of nodes inside the influence-domain for CCCC case. Credits: (Farahani et al. 2015)

"To both graphs it was added an adjustment curve using the moving-least squares with a cubic polynomial basis – "cubic approximation". These curves are adjusted to the RPIM values, and show the solution trend. In Figure 11 and Figure 12, it is visible that the minimum of the cubic approximation function is obtained on the vicinity of $N_I = 20$. Thus, future examples in this work, in axisymmetric, are analysed considering $N_I = 20$ nodes inside each influence-domain." (Farahani et al. 2015)

But for the remaining examples will be followed the advice for 2D *plane stress* of other authors, N_I = 16 (Belytschko, Lu, and Gu 1994) (W. K. Liu, Jun, and Zhang 1995) (Atluri and Zhu 1998) (Wang and Liu 2002a) (Nguyen et al. 2008) (Belinha 2014).

5.1.4. RPIM Behaviour with Irregular Meshes

"It is important to determine the influence of the mesh irregularity on the RPIM performance. Thus, this subsection studies the behaviour of the RPIM when random irregular nodal meshes are used in the analysis." (Farahani et al. 2015)

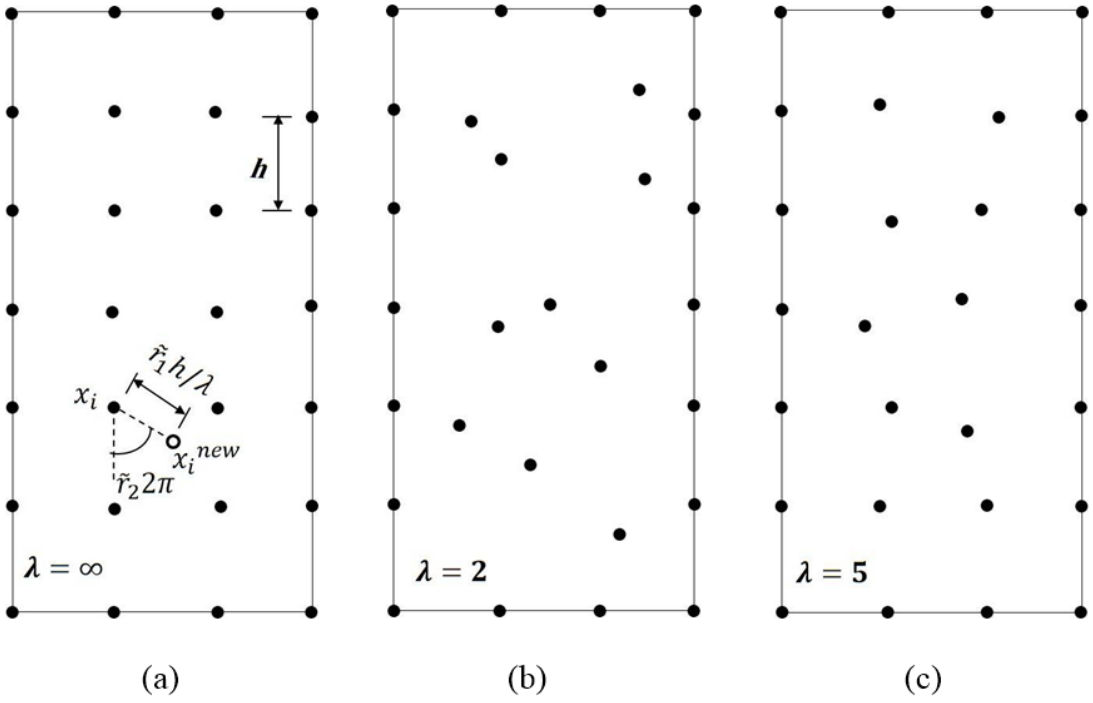

Figure 13 - (a) 7×4 regular mesh, (b) irregular mesh with λ=2 and (c) irregular mesh with λ=5. Credits: (Farahani et al. 2015)

"In order to generate an irregular mesh the following procedure is considered. First, a regular mesh is constructed, with all nodes equally spaced and aligned as the mesh example in Figure 13(a), afterwards all the nodes $\boldsymbol{x} \in \Omega \setminus \Gamma$ are affected with,

$$\begin{aligned} x_i^{new} &= x_i + \frac{\tilde{r}_1 \cdot h}{\lambda} cos\left(2\tilde{r}_2 \cdot \pi\right) \\ y_i^{new} &= y_i + \frac{\tilde{r}_2 \cdot h}{\lambda} sin\left(2\tilde{r}_2 \cdot \pi\right) \end{aligned}, \qquad \textbf{5-5}$$

being $\boldsymbol{x}_i$ the initial coordinates of node n_i, $\boldsymbol{x}_i^{new}$ the new coordinates obtained for node n_i and h is the inter-nodal distance shown in Figure 13(a). The random coefficient is defined by $\tilde{r} \approx N(0,1)$ and λ is a parameter that controls the irregularity level of the mesh. The effect of the irregularity parameter λ is shown in Figure 13. Notice that if

$\lambda = \infty$ the mesh is perfectly regular, Figure 13(a), and with the decrease of λ the mesh becomes more and more irregular, Figure 13(b) and (c)." (Farahani et al. 2015)

"The same circular plate described in the previous subsection was analysed considering several irregular nodal meshes with $n_r \times n_z = 81 \times 5$ nodes, varying the irregularity parameter from $\lambda = 100$ to $\lambda = 2$. Each constructed irregular mesh was used to analyse the problem considering the RPIM. The obtained results are presented in Figure 15 for the SSSS circular plate case and in Figure 14 for the CCCC circular plate case." (Farahani et al. 2015)

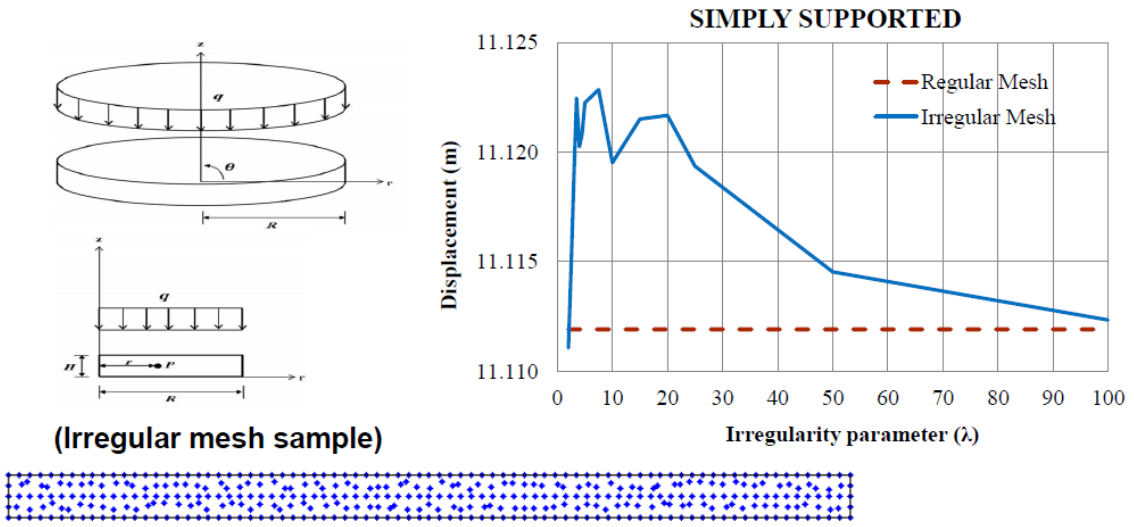

Figure 15 - Transversal center displacements obtained from RPIM varying the irregularity parameter for the SSSS case. Credits: (Farahani et al. 2015)

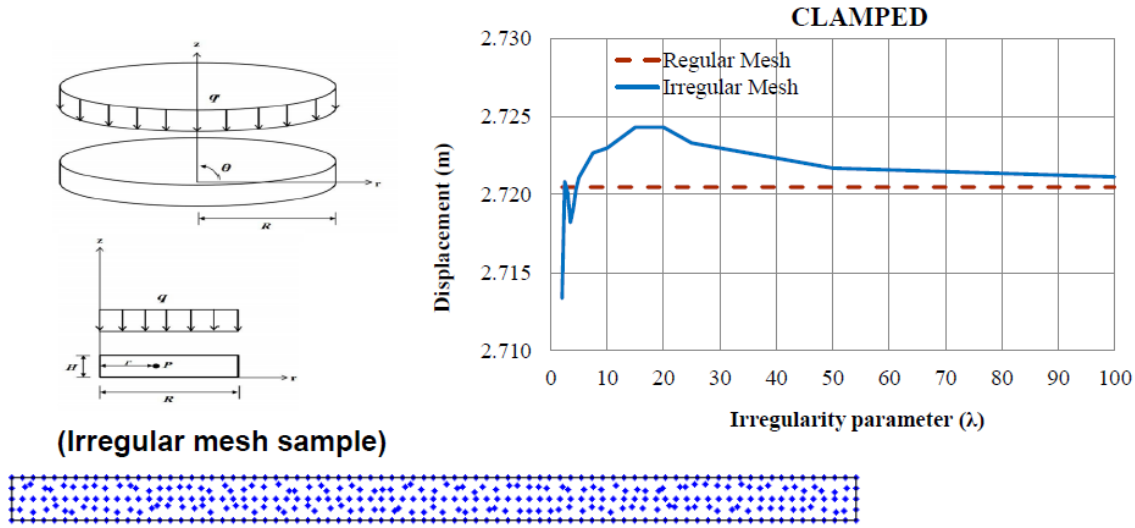

Figure 14 - Transversal center displacements obtained from RPIM varying the irregularity parameter for the CCCC case. Credits: (Farahani et al. 2015)

"The results show that the SSSS and CCCC solutions only start to show significant instabilities for meshes constructed with $\lambda < 4$, which are in fact extremely irregular meshes. For $\lambda \geq 4$ the results are stable and accurate. This example shows that, for the axisymmetric formulation, the RPIM permits to obtain accurate results using highly irregular meshes, therefore showing robustness." (Farahani et al. 2015)

5.1.5. Variation of R/H

"In this section several R/H ratios are considered and analysed. Consider the generic circular plate under the UDL $q = 100N/m^2$ presented in Figure 6. Four distinct circular plates are considered, each one with a distinct radius $R = \{10, 20, 50, 100\}m$ and all of them with the same thickness $H = 1.0m$. Thus, each of the four circular plates is analysed considering the RPIM and the FEM with axisymmetric formulation." (Farahani et al. 2015)

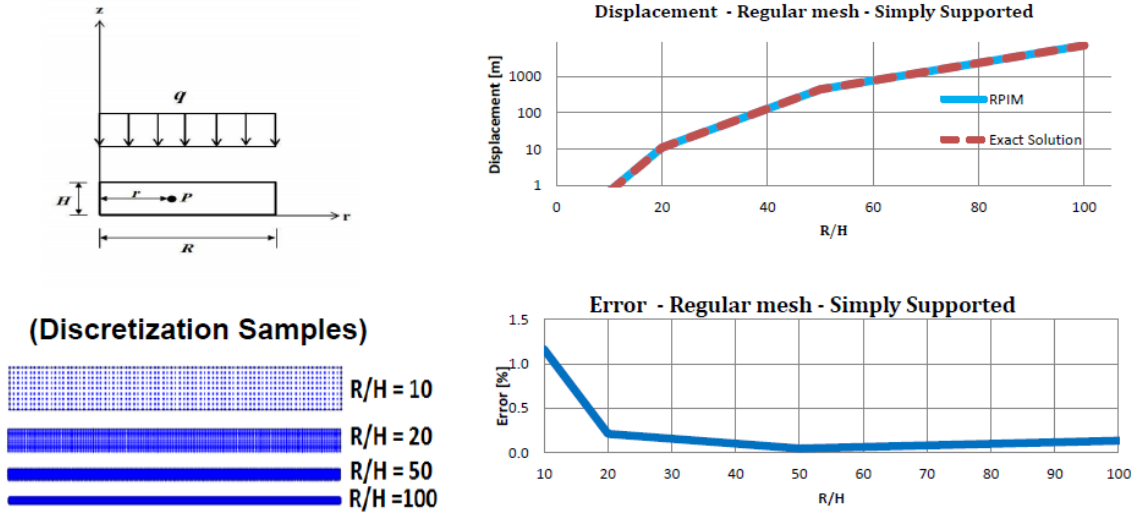

Figure 16 - Transversal displacement values obtained with the variation of the R/H ratio for the SSSS case. Credits: (Farahani et al. 2015)

"The results regarding the SSSS circular plate are presented in Figure 16 and the results obtained for the CCCC circular plate are shown in Figure 17." (Farahani et al. 2015)

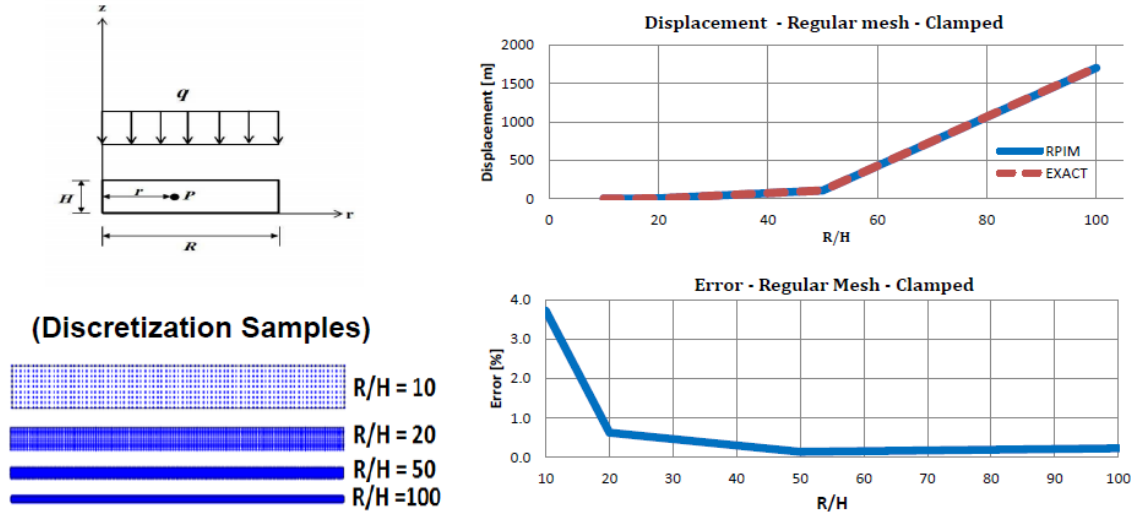

Figure 17 - Transversal displacement values obtained with the variation of the R/H ratio for the CCCC case. Credits: (Farahani et al. 2015)

"Both figures show that the RPIM solution is very close with the exact analytical solution and the FEM solution, permitting to demonstrate the RPIM accuracy." (Farahani et al. 2015)

5.2. Plain Concrete Beam under Three Point Bend Test

In this Subsection a three point bend test is introduced with all relevant configuration from selected work references, (Voyiadjis and Taqieddin 2009) (J. Malvar 1988), originally from Malvar and Warren (1988) . The plasticity model of concrete was omitted, so only elastic behavior or isotropic damage evolutions are considered in each gauss point. The damage evolution applied was the Oliver's law, (Polanco-Loria and S¢rensen 1995) (Cervera, Oliver, and Manzoli 1996). For the single edge notched plain concrete beam are used the following material properties: E = 21.7x10^9 Pa, f_c^- = 29.0 MPa, f_0^+ = 2.4 MPa, G_f^+ = 35 N/m. The full real test configuration is as illustrated in Figure 18.

Table 2 - Material properties for the concrete model used in analysis

Material	Young modulus, E [GPa]	*Ultimate compressive Stress,* f_c^- [MPa]	*Ultimate Traction Stress,* f_0^+ [MPa]	G_f^+ [N/m]
Concrete	21.7	29.0	2.4	35

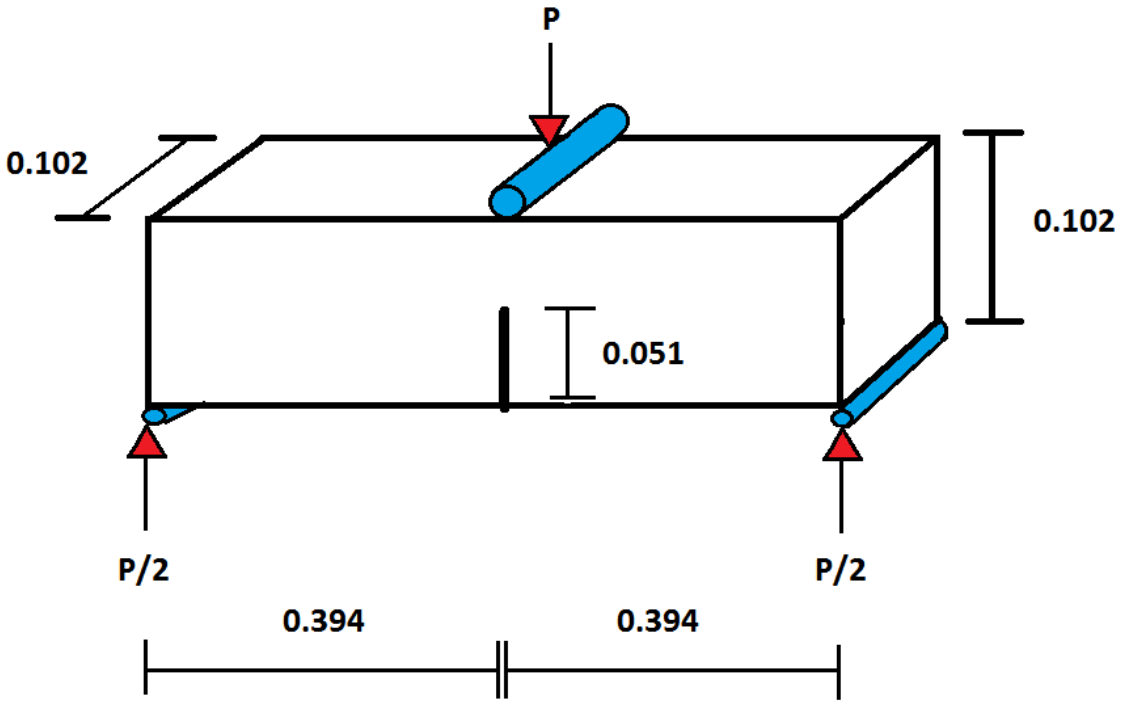

Figure 18 - Single-edge-notched beam subjected to three point bending test. Geommetry layout, (unit = m)

Given the symmetry of the geometry and boundary conditions, Figure 18, and for computational efficiency, only the half left part the geometry is considered. Also for efficiency a plane stress approach is adopted as schematized in Figure 19.

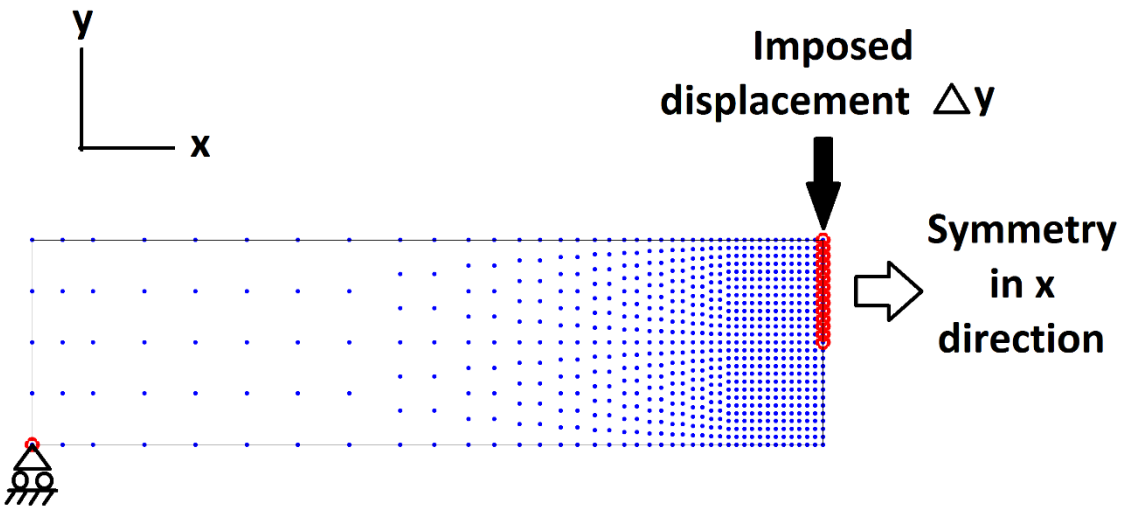

Figure 19 - Nodal disposal (mesh of later converged study). And meshless setup of plane stress approach in plain concrete.

Imposed displacement is used ($0.5x10^{-3}$ m at total). This decision avoid *snap through* 'black out' zone or any similar related convergence singularity. With this setup it was possible to continue using a modified Newton-Raphson scheme. The characteristic length, $l_{CH} = 12.6 \times 10^{-3}$ m, was used. A special and simple use in this work was made of the l_{CH}. Always was guaranteed that close to a gauss zone that have traction damage, the average nodal distance was equal or less than l_{CH}. For the calculation of the A^{+} was always used the value $l_{CH} = 12.6 \times 10^{-3}$ m regarding the corresponding equation 2-17 or equation 4-18. This makes of this model one of the simplest available and with corresponding low computational cost.

For the referred nodal disposal, Figure 19, a 'background' integration mesh, Figure 20, was implemented in order to compute a solution in a much balanced way possible.

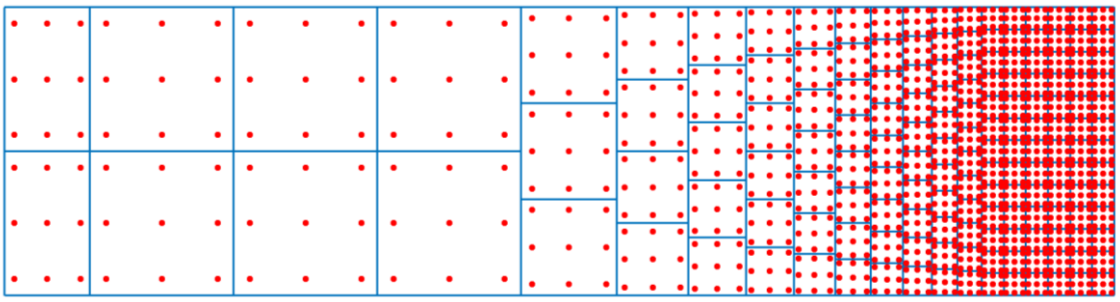

Figure 20 - Integration mesh implemented for nodal disposal of Figure 19

The Figure 19 and Figure 20 are a good example of flexibility of RPIM formulation regarding coarsening or refinement. The integration mesh is almost completely formed of square cells which conducts to more accurate results. The nodal disposal just follows this pattern but with some more convenient adaptation resulting from refinement/coarsening orientation. We can recall that FEM in this same case would have inconvenient distortion of elements, generalized aspect ratios different from unit, or hanging nodes.

The Influence domain of one arbitrary Interest Point (I.P. has the same coordinates of each gauss) is shown in Figure 21. For each I.P. is made a search for their

16 closest nodes in a radial sense. Meaning that, each I.P. first tries that search with a relatively small arbitrated radius. If it does not find 16 nodes for that radius size the radius is increased by an arbitrated percentage successively till all 16 nodes are found for that Interest Point.

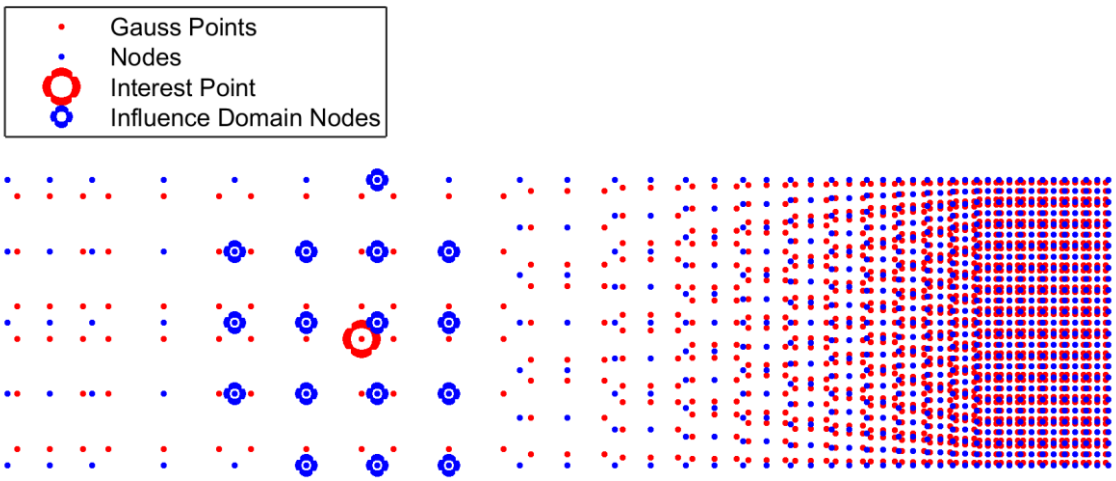

Figure 21 - Example of the (Radial) Influence Domain Nodes of one arbitrary Interest Point of the current configuration

5.2.1. Convergence study

Here the most exclusive parameter that is intended to study is the refinement of the mesh especially close to the notched tip and forward up. Any other possible way of conditioning the results was avoided, namely great refinement jumps or any irregularity. This way the results can capture more accurately the outcome of refinement alone.

As concluded from the elastic convergence study resumed in Figure 7 and Figure 8, the acceptable number of nodes through a given thickness is 5 nodes (more than enough in the axisymmetric examples). That result is assumed here for starting the study. No traction damage or compression damage were ever developed close to the left boundary of the RPIM geometry. Actually the damage through all study was registered comfortably in the last 5 % zone area of the geometry in the x-direction. All trials used N_{LEFT} = 5 nodes through y-direction in the left edge. The number of nodes of the right edge, through the y-direction, in all the trials was N_{RIGHT} = {5, 7, 9, 11, 13, 15, 17, 19, 21, 23, 25, 27, and 29}.

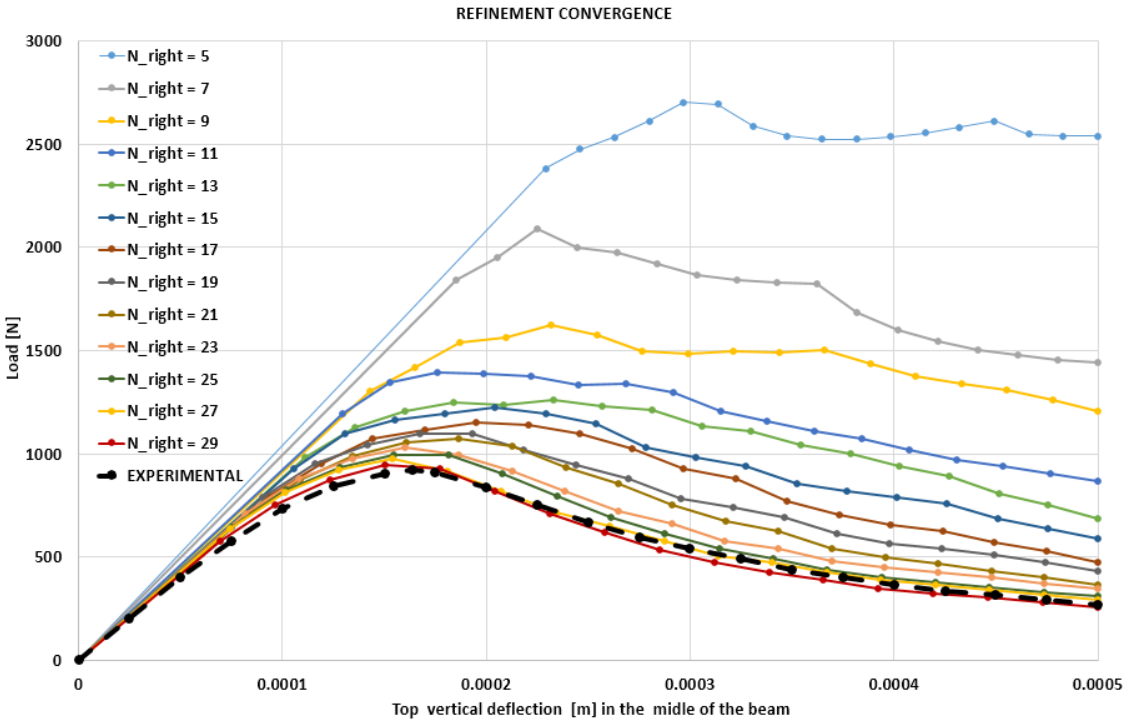

Figure 22 - Refinement convergence study

In the present study both N_{RIGHT} = 27 or N_{RIGHT} = 29 are extremely acceptable discretization choices in terms of accuracy of the results of the solution for these particular boundary conditions. And one would prefer use N_{RIGHT} = 27 given the better computational efficiency it can provide. This detailed data base represented in Figure 22 strongly suggests the converged curves are a numerical stable trend rather than a random or casual computation.

5.2.2. Variable Fields Relevant to Damage Phenomenon

Given the symmetry of the boundary conditions and the pre-notch, the starting place of at least one crack (or the principal major or macro crack) is expected to be at the top of the notch. In similar conditions an average vertical crack evolution is expected to occur like the one shown in Figure 23, where we see a real experimental crack of a bending test.

Figure 23 – Vertical crack disposal resulted from a 4 point flexural test. Credits: http://www.controls-group.com

The present work doesn't cover an explicit crack evolution. But still the damage field (mostly in traction) shows a pretty close fair guess of where it is expected to occur a crack.

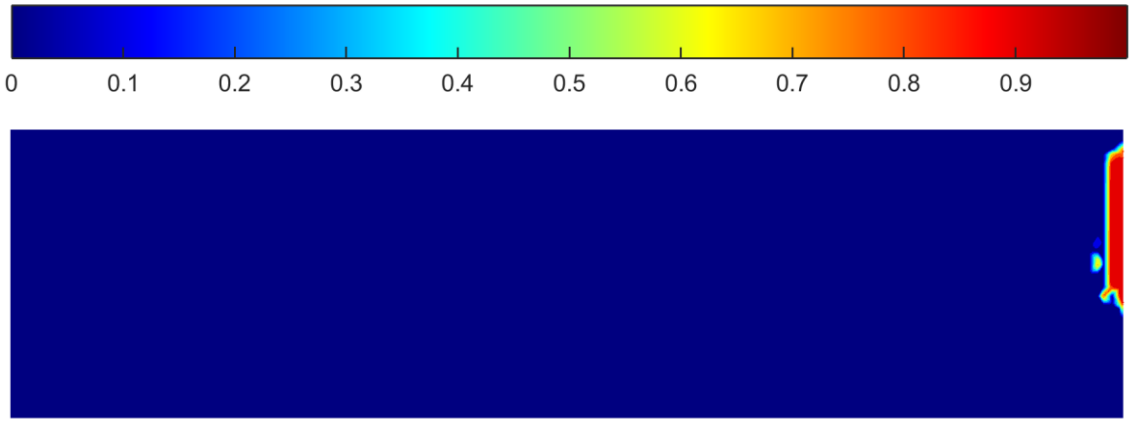

Figure 24 - Traction Damage field at the final step for plain concrete

Figure 24 shows that the maximum (actually the exclusive damage) is located in the same equivalent zone as the crack of Figure 23 and similarly to the damage fields (generated at *Abaqus* software) of the already referenced work (Voyiadjis and Taqieddin 2009) from which the present setup was mostly guided.

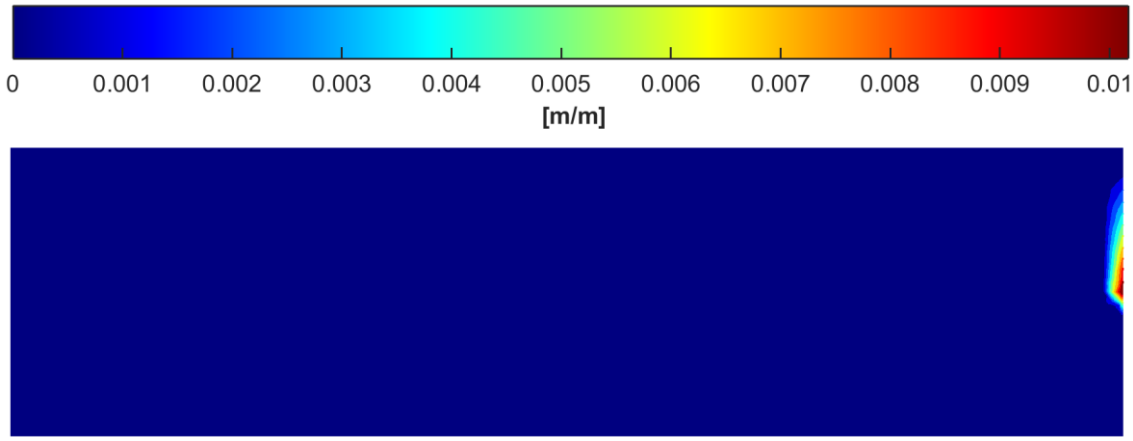

Figure 25 - Traction Strain at the final step for plain concrete. Nonlinear regime

Figure 25 shows exclusively Traction Strain field where a major zone (almost 100% of frontal area of geometry) presents a rigid body behavior and a very thin but relatively extended vertical zone up of the notch tip with high traction strain values. In an only elastic analysis we would expect stresses to occur in just obvious geometric spots

candidates to concentration of stresses. This can be observed in Figure 26 where the most intense stress is confined in a round spot close to initial geometric configuration.

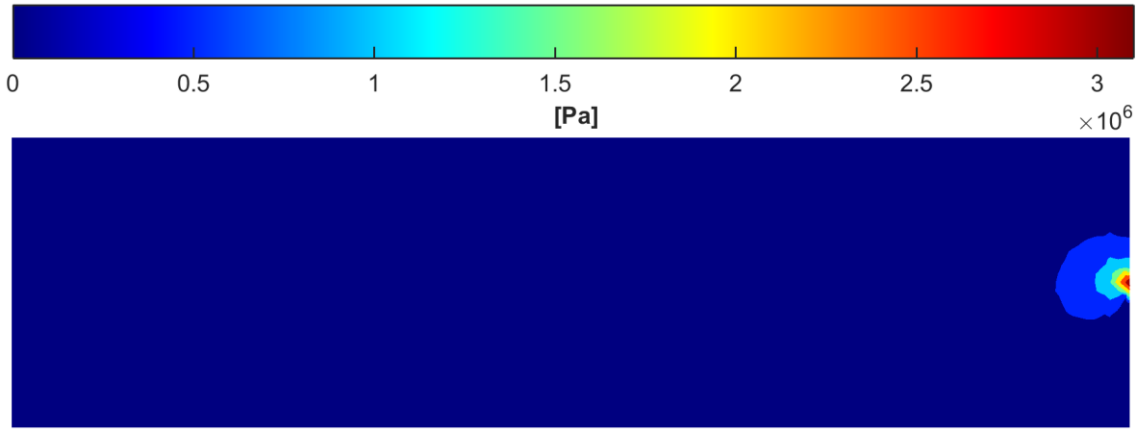

Figure 26 - Traction stress field before yield. Here only elastic regime.

But when we start the yielding point (let's say till the full imposed displacement) the routine of damage and the Newton Raphson process make correction in traction stresses of the gauss points and consequently in the entire Cartesian stress components due to softening. So in damage simulation as we saw previously the strain fields are a bit less notorious than elastic strain fields maximum value zones. But the stress fields are even less correct to guess where they might occur in their maximum values as we can testify from observe Figure 27.

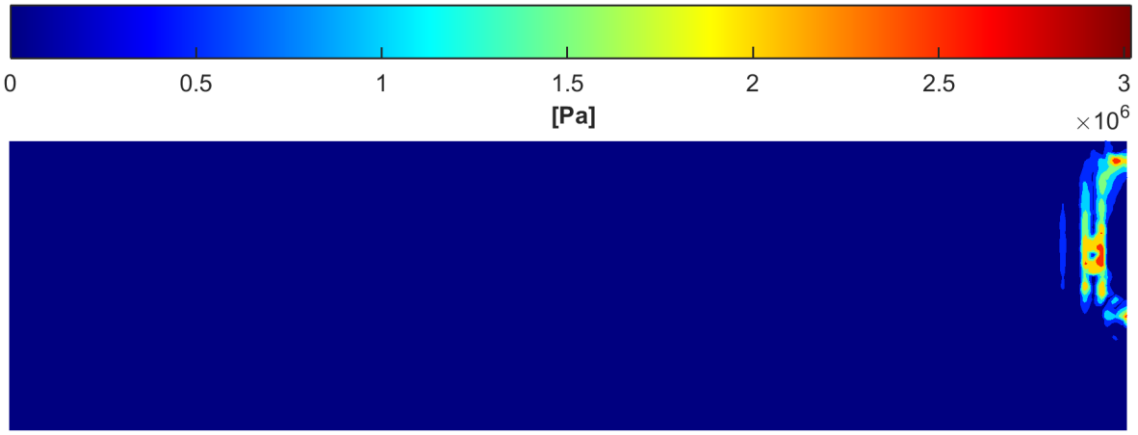

Figure 27 - Traction Stress final step for plain concrete. Nonlinear regime. Evident 'relax' of stresses.

Different from the fields in elastic regimes, after damage strain fields, Figure 25, cannot be easily guessed from direct geometric critical spots. Also stress fields, Figure 27, show a not obvious correlation with the correspondent strain fields. This observations apply to traction strain or stresses because the model law of traction damage is brittle. Once one gauss point starts yielding in traction the law evolution is an immediate decrease in stress value, Figure 28. Compression stress law evolution, in the other hand, is ductile. Compression stress continues to increase in value (absolute) even after yielding begins and remains in that increase for a certain range of compression strains before finally starts to decrease in value (absolute).

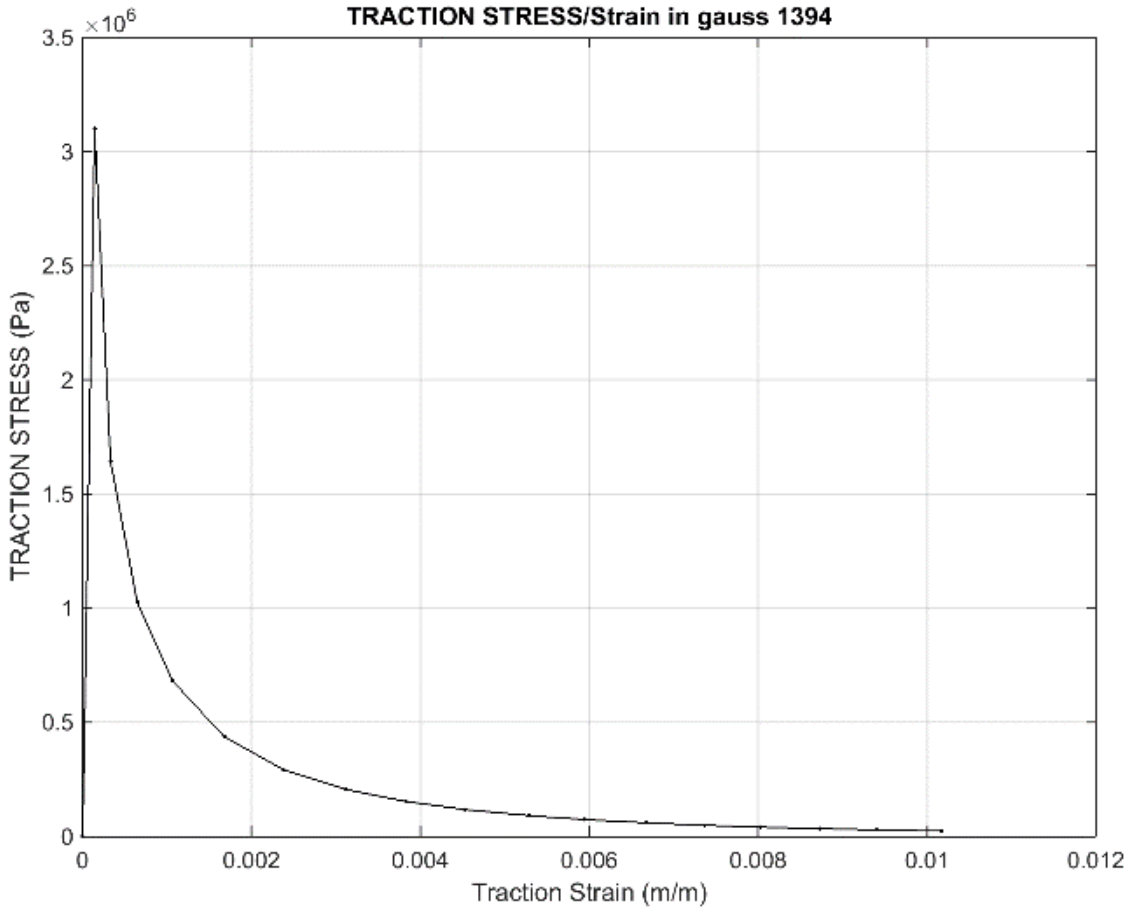

Figure 28 – Curve of traction stress against traction strain of one random yielded gauss point of the simulation

Again as we previously watched in the traction strain field, the displacement field follows the same pattern showing a correspondent geometric agreement. We are seeing in Figure 29 a general rigid body behavior (almost all geometry) except a localized and organized separation of nodes in a cracked shape. This is fairly a similar brittle crack shape to the one showed in a typical experimental bending test, Figure 23.

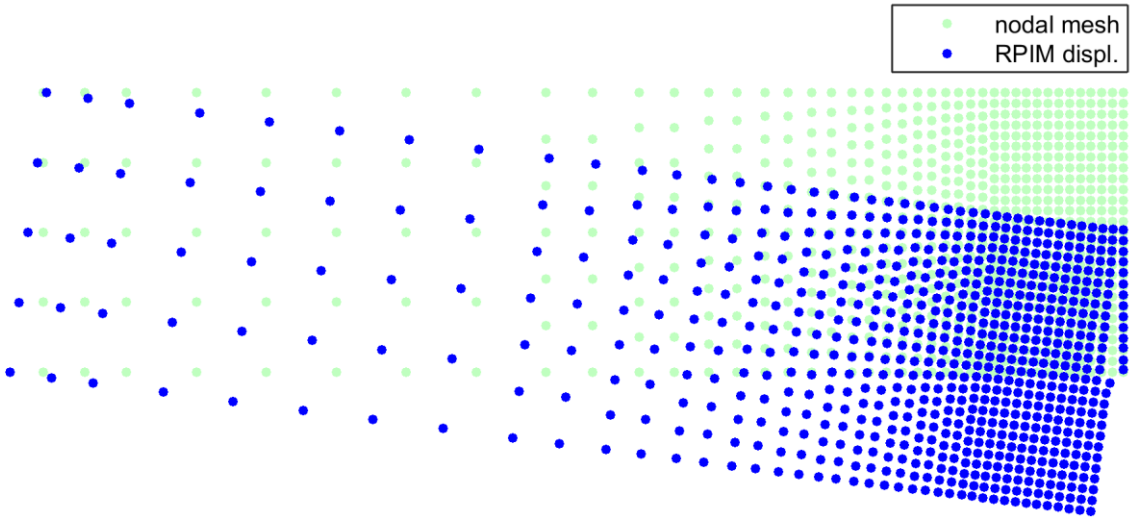

Figure 29 - Displacement field final step, nonlinear regime, for plain concrete. Magnified 100 times

In the iterative process the explicit correction of stresses conducts to an internal force vector (some nodal DOF different from zero) which will be unbalanced in relation to the external force vector (present work is only zeros, because is imposed displacement approach). This will lead to a residual vector that induces gradual increase of a crack or intense localized traction strains. Only when the relative residual absolute value is less than $1x10^{-6}$ the calculations are allowed to move to next step increment.

5.2.3. Damage Law Behavior with irregular meshes

The same boundary conditions are used here as in the subsection 5.2.1. Only the N_{RIGHT} = 27 is considered and the irregularity parameter is set as λ = 1, more severe than the already studied in subsection 5.1.4. Ten trials are simulated and since the nodal irregularity is governed by a random process, some variation on the results are also expected. Figure 30 shows one sample of the 10 random nodal disposals.

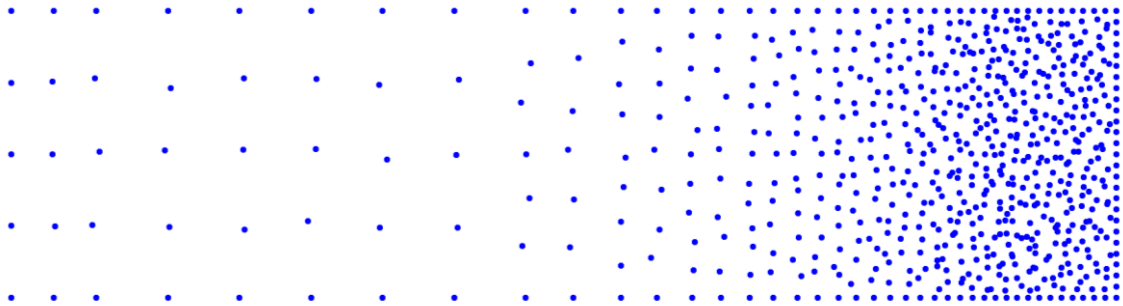

Figure 30 - Sample of one of the 10 trials of random irregular nodal disposals with λ = 1.

In the Figure 30 one can observe that the irregularity effect is more intense in the zone we expect more nonlinearity (with damage evolution law) and less intense in the zone we expect just the linear elastic behavior. This is completely intentional. Allowing elastic only zones to pass simultaneously through that harsh test could prevent somehow to capture the real robustness of damage law alone. Again as in any study one should isolate the variables as much as possible we want to test. If so we can eventually move on to further complex conditions.

And also RPIM allows the integration mesh to be exactly as shown in Figure 20.

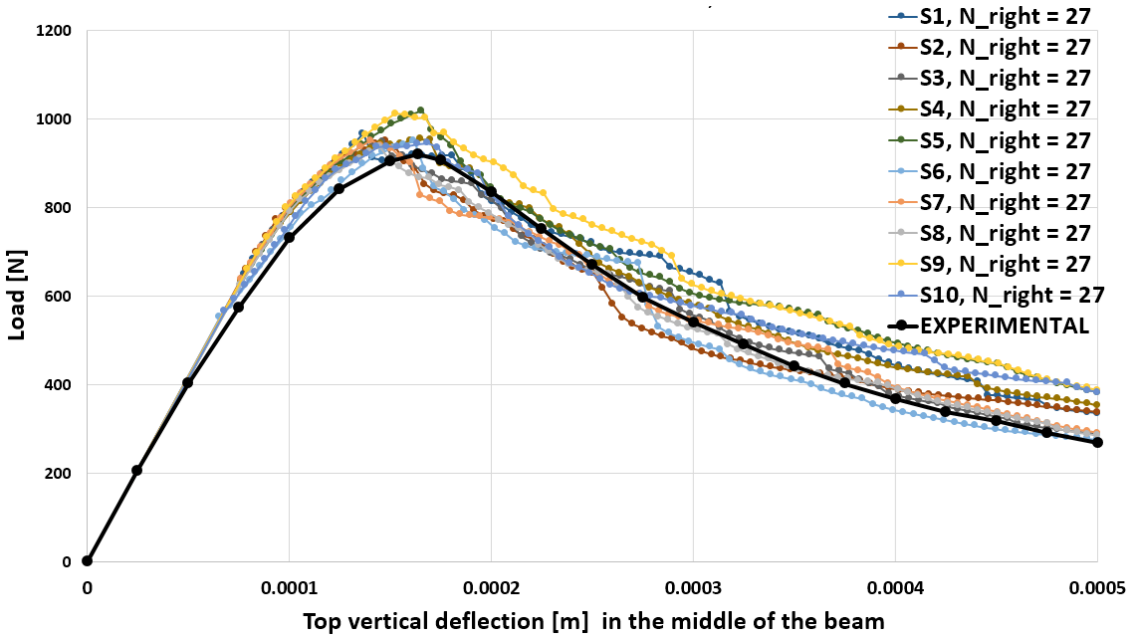

Figure 31 - Load vs deflection curves of 10 samples of high irregular nodal disposal

Given the relevant nonlinearity of a numerical routine like a damage law we can say that the curves show RPIM can have remarkably stable behavior even when nodal disposal is highly irregular. Also the damage algorithm as guided by Cervera et al. (Cervera, Oliver, and Manzoli 1996) (Faria, Oliver, and Cervera 1998) work shows to be much suitable to this static isotropic example even in this not ideal nodal set ups.

5.3. Reinforced Concrete Beam under Four Point Loading Test

The set up parameters for the analysis developed in this subsection is based on the work of *Ibrahim M. Metwally*, (Metwally 2015), mostly the boundary conditions outlined to analyze a four point load bending test. The reinforced concrete beam is made of common concrete (matrix) and *Glass Fiber Reinforced Polymer* (*GFRP*) rebar. The correspondent material properties are presented in Table 3 and Table 4.

Table 3 – Experimentally measured material properties of concrete for reinforced concrete analysis

Material	Young modulus, E [GPa]	*Ultimate compressive Strength,* f_c^- [MPa]	*Ultimate Tensile Stress,* f_0^+ [MPa]	*Tensile Fracture Energy*[1], G_f^+ [N/m]	*Poisson ratio, v*
Concrete	23.02	40.0	2.1	35	0.2

Table 4 - Experimental tension test results of the used GFRP rebar

Material	Young modulus, E [GPa]	*Failure Stress,* f_c^- [MPa]	*Poisson ratio, v*	*Bar diameter [m]*	*Cross section area* $[m^2]$
Glass Fiber Reinforced Polymer, GFRP	41.1	709	0.26	0.019	0.322×10^{-3}

The applied boundary conditions were as schematized in Figure 32 and with an imposed displacement approach. The imposed displacement applied in the top load 'support' was the necessary to displace 0.0125 m vertically the middle of the beam.

[1] 35 N/m ended up to be arbitrated due to absent indication of either the characteristic length, l_{CH}, or the tensile fracture energy, G_f^+, at the source work, (Metwally 2015).

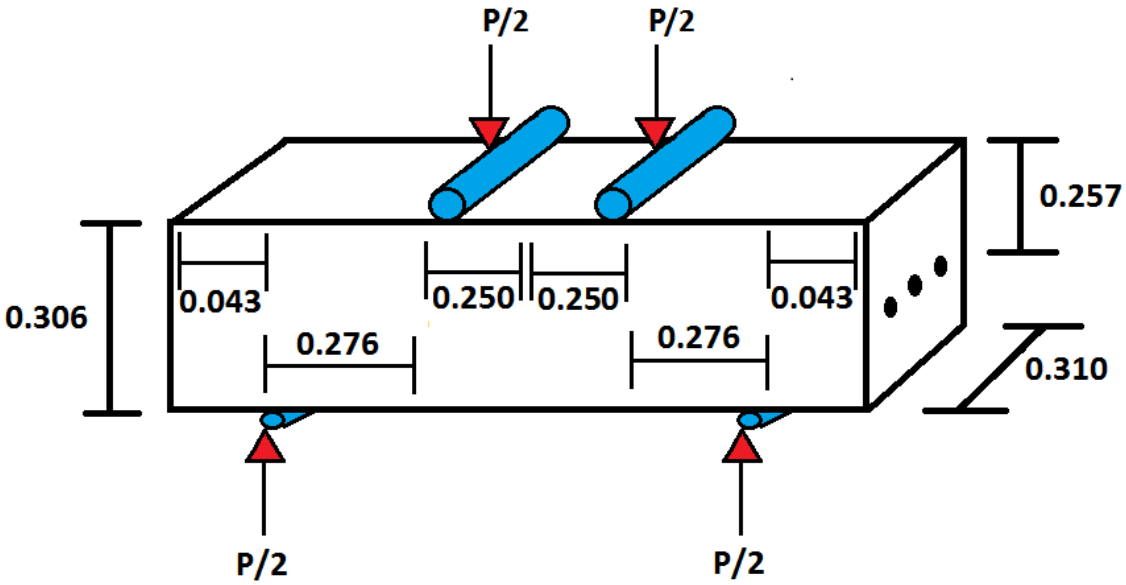

Figure 32 – Reinforced concrete beam subjected to four point bending test. Geometry layout, (unit = m)

Given the symmetry of the geometry and boundary conditions, Figure 32, and for computational efficiency, only the half left part the geometry is considered. Also for efficiency a plane stress approach is adopted as schematized in Figure 33.

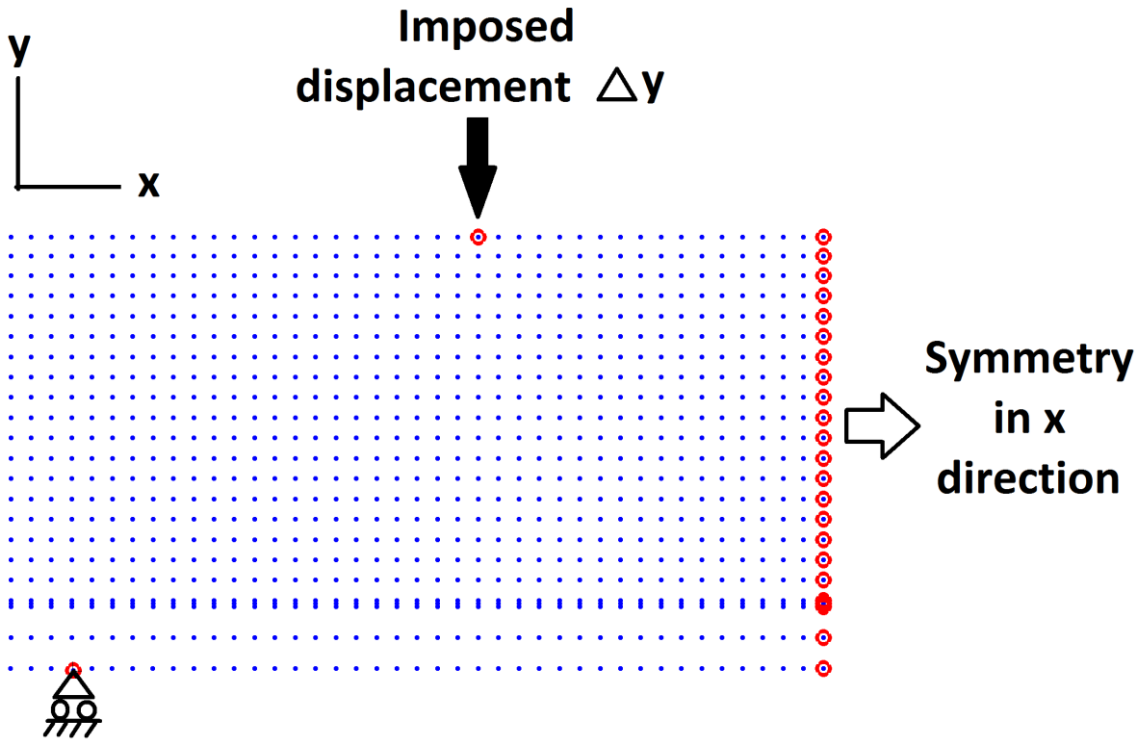

Figure 33 - Nodal disposal of final accepted result. And RPIM setup for plane stress approach in reinforced concrete study.

Some rebar cross section equivalency was needed to implement for guaranty of the closest results possible between this simplification (2D plane stress) and any other legitimate approach (3D or beam theory). This is schematized in Figure 34.

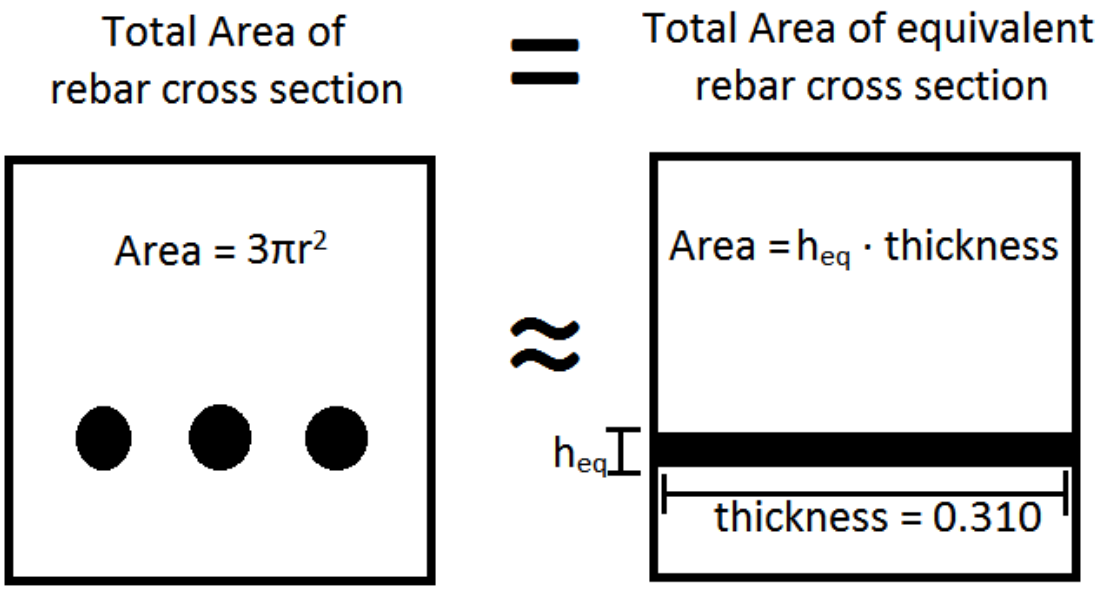

Figure 34 - Correspondence between cross section area and equivalent area of rebar for 2D plane stress simplification.

For the referred nodal disposal, Figure 33, a 'background' integration mesh, Figure 35, was implemented in order to compute a solution in a much balanced way possible.

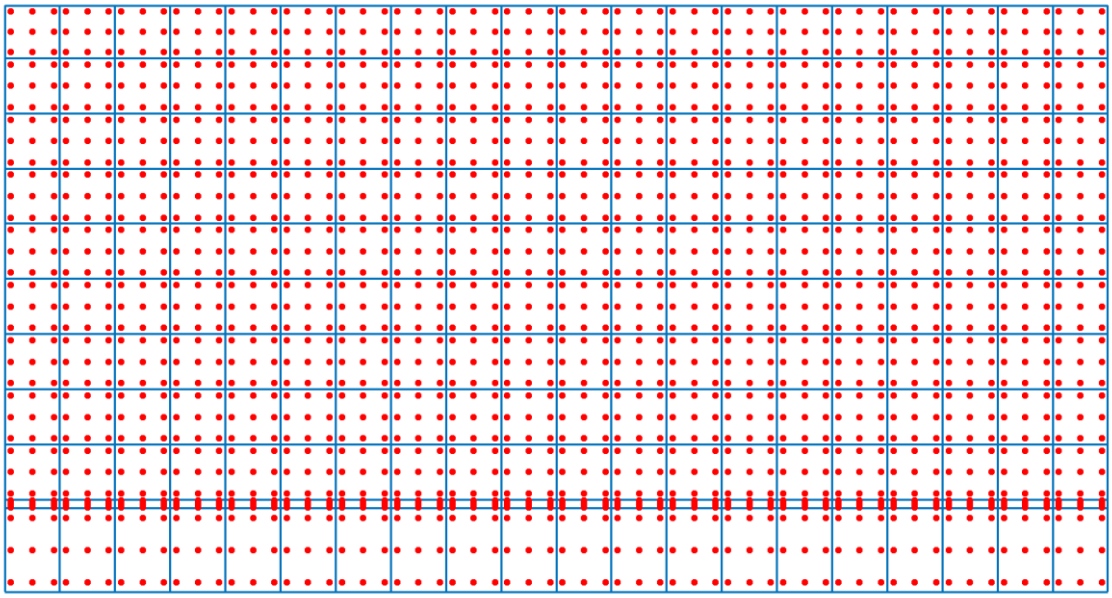

Figure 35 - Integration mesh implemented for nodal disposal of Figure 33.

In the integration mesh we observe a narrow row of integration cells. Those are set with the rebar material properties. So in stiffness matrix whenever those gauss are 'called' they put the correspondent contribution to that matrix following their constitutive properties of the 2D rebar simplification in a plane stress approach.

5.3.1. Numerical Versus Experimental Results

The iterative routine setup for this work was fully prepared to plasticity evolution law with a plasticity subroutine for reinforcement rebar. Given, partially, to the relatively high failure/ultimate stress values for the reinforcement rebar and, partially, to the specific boundary conditions such failure values were never reached for rebar in any of the trials for this work. Examples available in literature for reinforced concrete are often absent of some particular parameters data that are crucial for the current damage algorithm. So, as an indirect consequence, the plasticity model was not effectively used for this specific example, because reinforcement of this beam has an elastic-failure behavior only.

Given the stability of RPIM in maintain accurate results even with harsh conditions such as the ones studied in subsection 5.1 in elastic regime, was assumed here that the high ratio integration cells and correspondent nodal disposal inside the rebar equivalent zone, were expected to produce low interference in the accuracy of results for this present test. Also remembering that rebar zone stayed always in elastic regime. That is, anyway, acknowledged and future detailed work should have this in consideration as well.

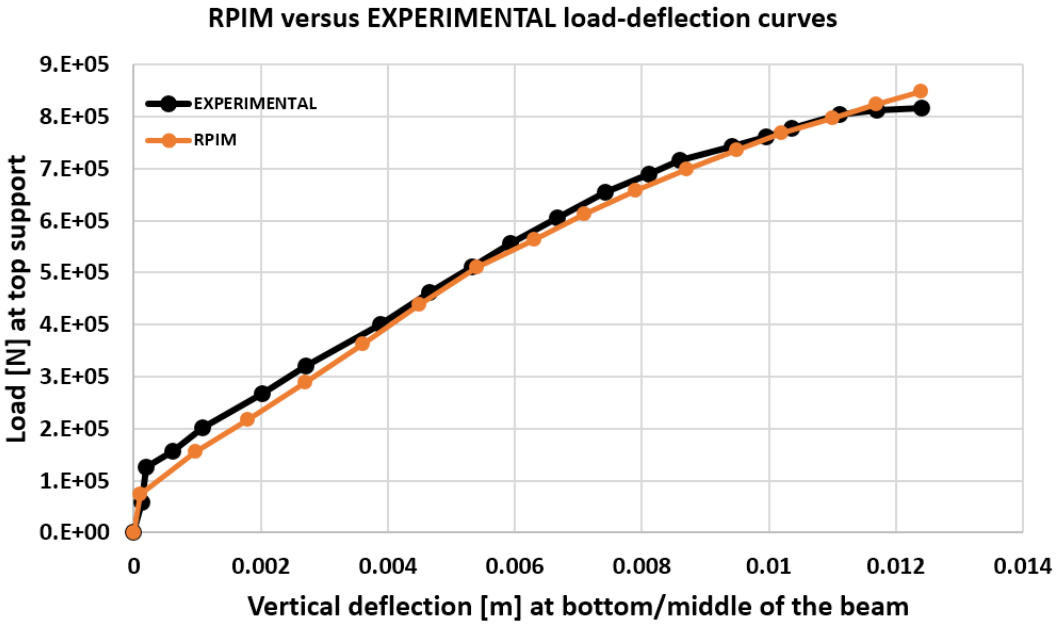

Figure 36 - RPIM versus experimental Load-deflection for reinforced concrete beam

Here no detailed convergence study was performed to support the final RPIM curve of load deflection achieved. But the low deviation (in shape and values) shown by RPIM curve profile from experimental results in Figure 36 give confidence of convergence achievement.

5.3.2. Variable Fields Relevant to Damage Phenomenon

We know here exists reinforcement to withstand high traction stress values, the configuration is a 4 point bending test and not a 3 point bending test. We know the absolute value of imposed displacement here is 12.5 mm and not 'only' 0.5 mm in section 5.2. Here we don't have a notched beam. This alone increases the complexity of what to expect qualitatively occur in the variable fields. Specially regarding the appearing of cracks is not well predicted unless the observer is experienced in this particular cases. The Figure 37 shows the real image record of the end of experimental test that I followed for this present section.

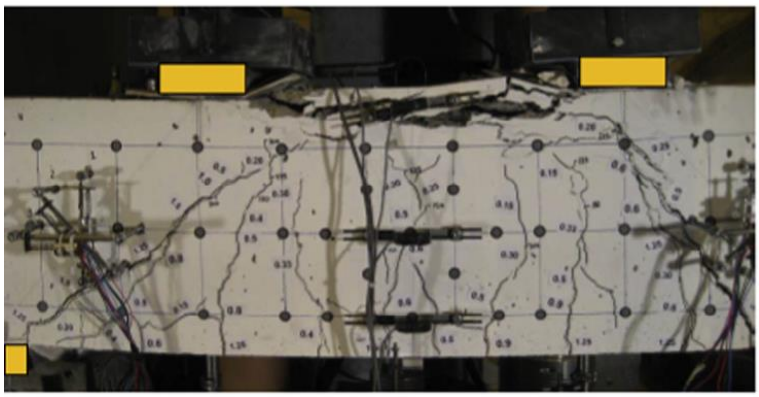

Figure 37 - Real image record of the experimental test used in the present subsection. Credits: (Metwally 2015).

Even in this real symmetric test there exists a not 'perfect' symmetry in crack propagation. I may identify at least 4 crack types. We can say the 'principal' cracks (the ones starting from the bottom) that are farthest from the middle zone are 45^{o} cracks (shear cracks). Also other 'principal' cracks in the middle are close to be vertical cracks ('pure' traction cracks). We also see in the top middle, horizontal cracks roughly due principally to compression damage phenomenon (compression cracks). With the previously mentioned cracks we need acknowledge in the real world traction or more accurately shear are the ultimate culprits of any crack development. And finally we can see random secondary cracks due to mesoscale defects in the concrete aggregate.

In the present work simulations it is possible to see a large damaged area instead of a set of well-defined crack lines, Figure 38.

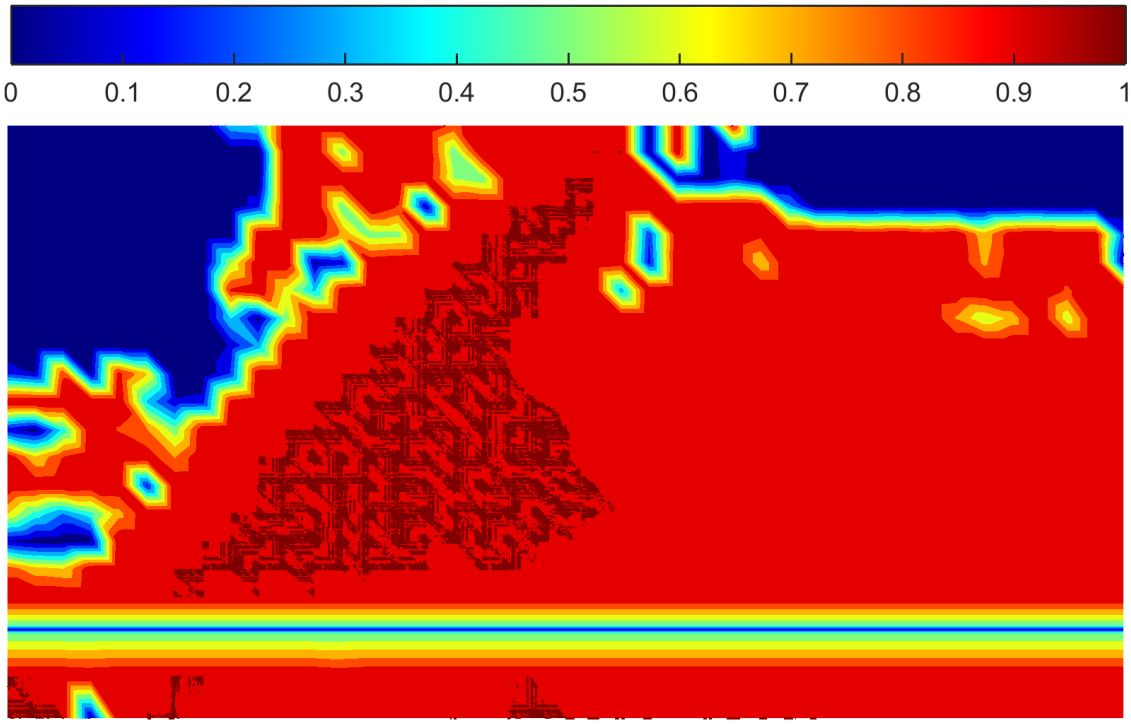

Figure 38 - Traction Damage field at the final step for reinforced concrete.

With this example it is clear that this routine of isotropic damage lacks of an explicit crack evolution path scheme. Instead the geometric boundaries within the all routine is considered as a whole entire single piece from the beginning to the last incremental step. This means that the continuum mechanics model is assumed and persists even in locations where the damage reached relatively high values. Future work should contemplate release of nodes from each other giving a more finite strains like approach.

This simulation led to compression damage to occur with considerable expression in the top of the beam, Figure 39.

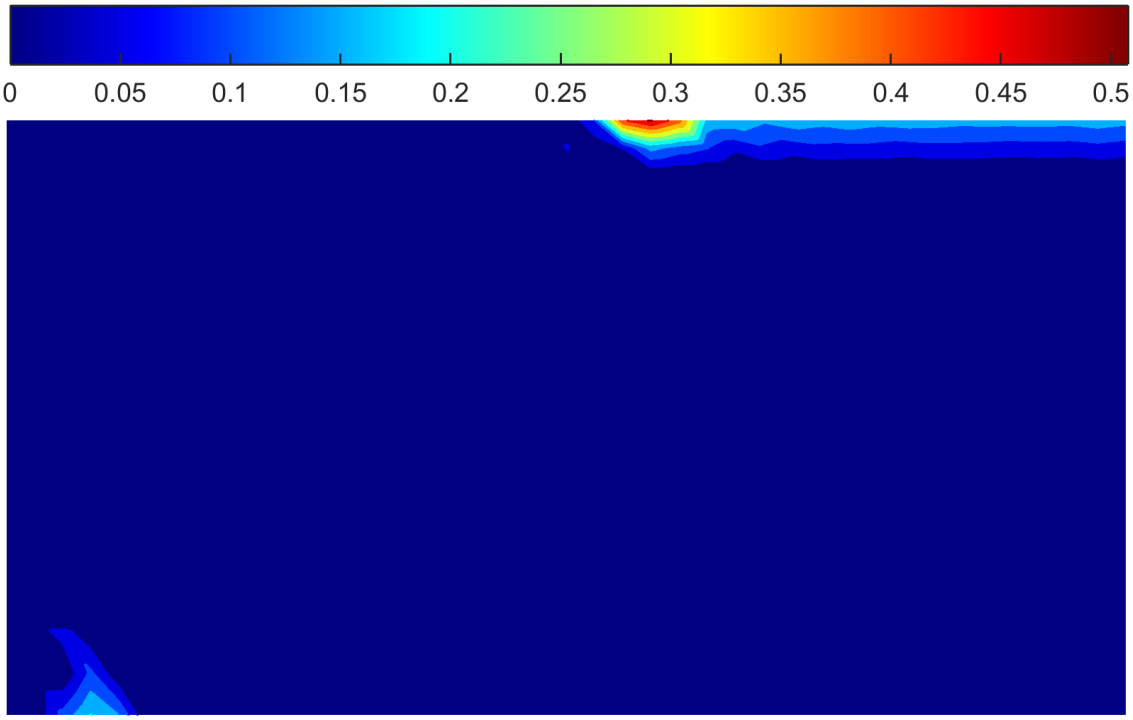

Figure 39 - Compression Damage field at the final step for reinforced concrete.

This top of the beam compression damage seem to be also coincident with the top beam horizontal cracks shown in Figure 37.

Also the traction strain field, Figure 40, shows agreement with the potential principal crack zones giving special relevance to a potential 45º crack. We can observe that this is also the case in Figure 37 where the 45º cracks are apparently more pronounced than the vertical ones.

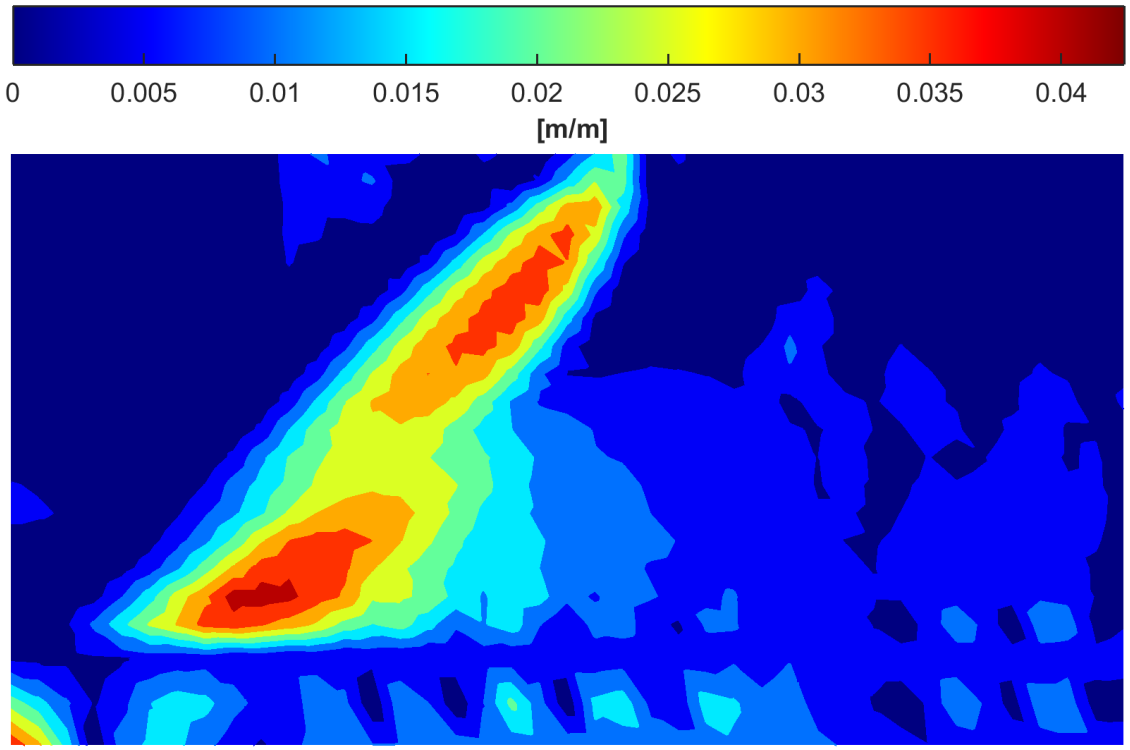

Figure 40 - Traction Strain field at the final step for reinforced concrete. Nonlinear regime

Even after compression damage occur, compression stress fields, Figure 41, are more intuitive than traction stress fields.

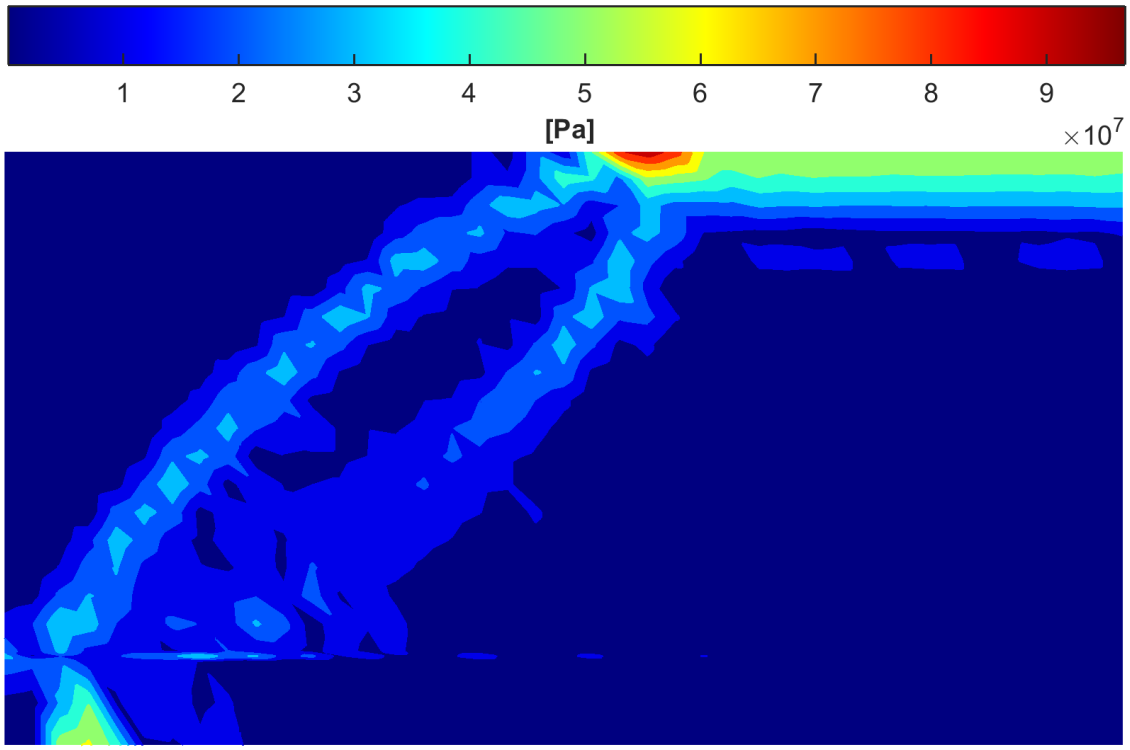

Figure 41 – Compression Stress final step for reinforced concrete. Nonlinear regime.

Till certain point or till some compression strain value, in each gauss point, compression stresses behave resembling an elastoplastic behavior. In that regimes those stresses keep increasing in value, Figure 42, despite certain increase rate decay. After compression stresses reach a maximum absolute value they begin to decrease following the fulfillment of the proper damage evolution law.

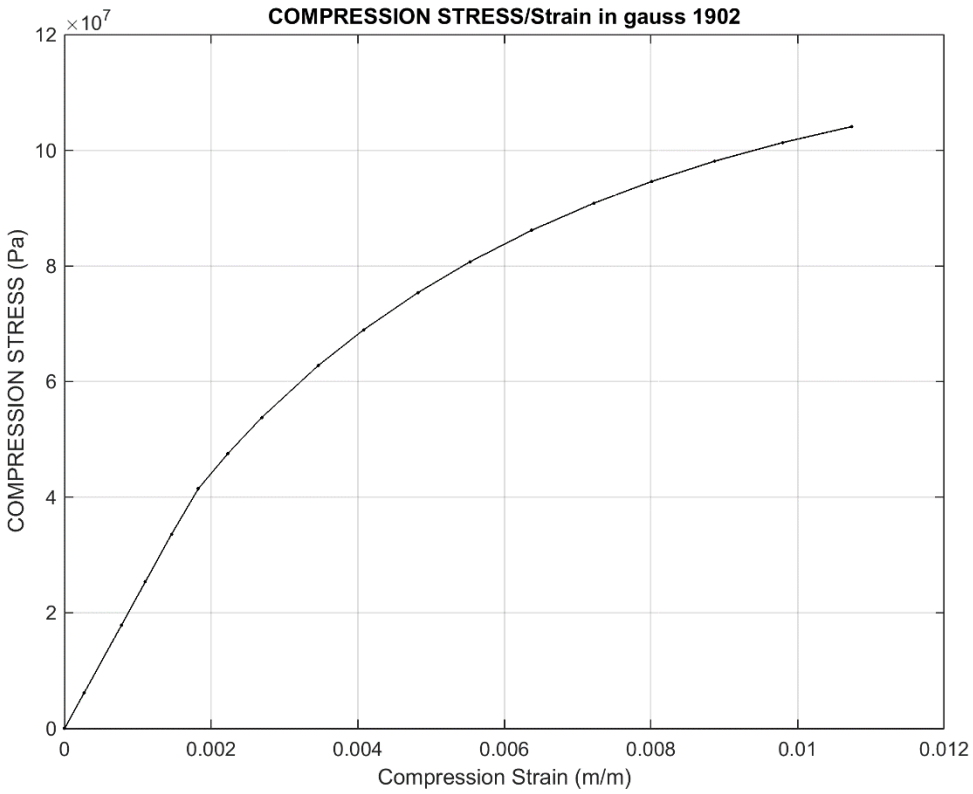

Figure 42 - Curve of compression stress against compression strain of one random yielded gauss points of the simulation

So, clearly, concrete compression damage model has a ductile like behavior opposite to the brittle behavior of traction concrete damage model, Figure 28.

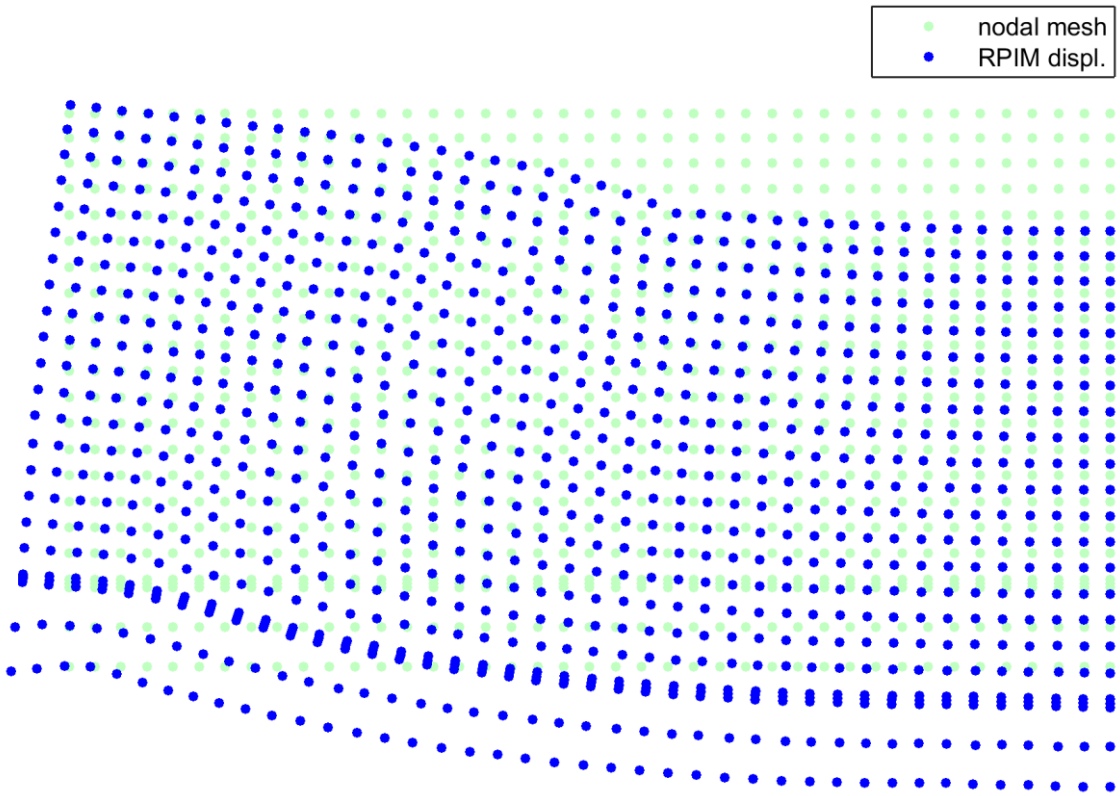

Figure 43 - Displacement field final step, nonlinear regime, for reinforced concrete. Magnified 15 times

As we can testify from Figure 43, the introduction of rebar or reinforcement in concrete leads to a displacement field with a more general ductile behavior opposite to plain concrete, Figure 29.

This relevant effect is more evident in von Mises stress field, Figure 44, where the higher stress values are exclusively concentrated in the rebar zone.

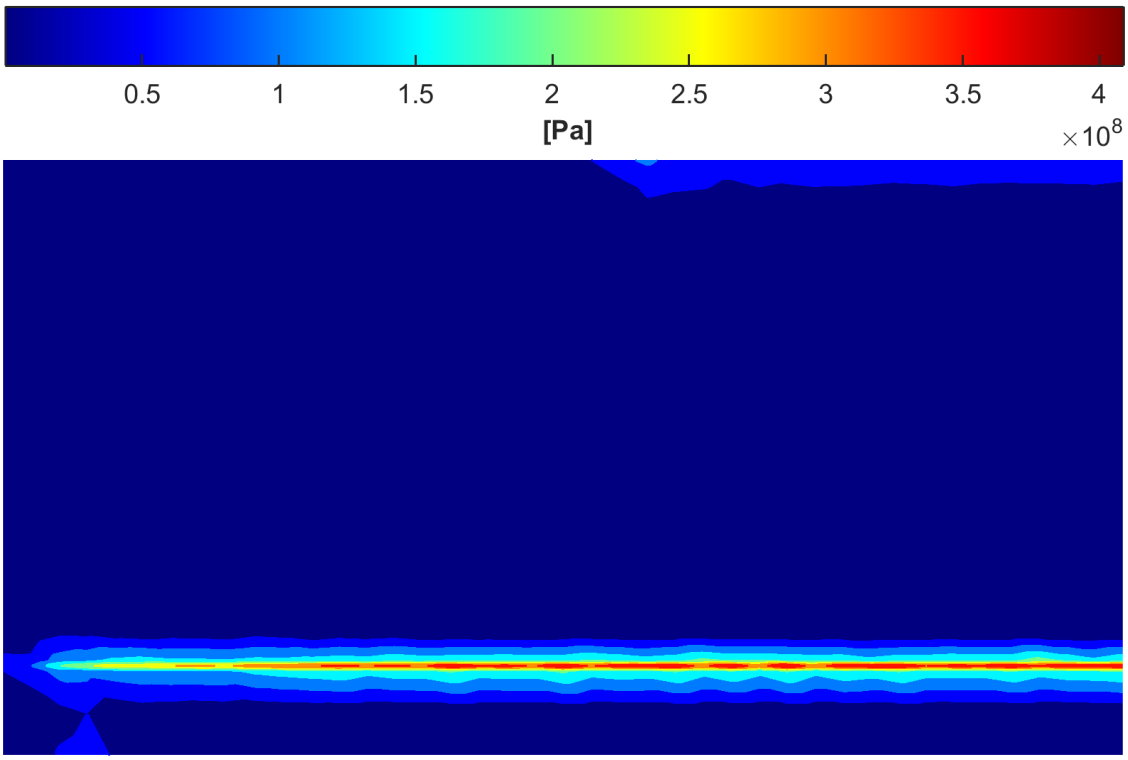

Figure 44 - von Mises Stress field for reinforced concrete. Nonlinear final step increment.

6. Conclusion

The many different studies performed at this present work show undeniable robustness of *RPIM*. It is a method that can accurately predict the mechanical behaviour of axisymmetric-type geometries competing fairly with giants of commercial software like *Ansys*.

The flexibility of *RPIM* is something we cannot forget. It potentially can deal with any kind of complex geometry shapes with a reasonable nodal disposal easily discretized without prohibitive rules to achieve it.

RPIM showed once more through this work, it is a method suitable to include a nonlinear material law in it and at same time reach real world experimental data results. Particularly with the damage law *RPIM* was tested and passed it with extraordinary accuracy.

Damage evolution laws were adapted at maximum possible from literature and even with slightly controlled changes, like the *characteristic length*, the results proved a robust implementation with accurate outputs. Also the different fields (and not just damage alone) showed that they are all important in order to detect the highest potential crack locations. Particularly the strain field showed almost invariable fairly acceptable accuracy when compared with real test images.

Future work should address a *mesh objective characteristic length* intense study and move to even more comfortable crack evolution prediction for *RPIM*.

6.1. Axisymmetric Circular Plates

The axisymmetric nodal convergence study indicates in both Figure 7 and Figure 8, that with only 5 nodes through thickness, RPIM presents less than 0.5% error. That study also indicates a fast convergence rate when compared with the exact solution.

The numerical integration scheme of 3x3 is a reasonable choice to many applications given an efficient proved performance allowing errors lower than 0.8%, evident from Figure 10.

For the particular axisymmetric implementation the most efficient number of nodes inside of an influence domain is 20, as verified in Figure 11 and in Figure 12.

Despite that useful fact, for *plane stress* was used 16 nodes inside each influence domain based in another studies (Belytschko, Lu, and Gu 1994) (W. K. Liu, Jun, and Zhang 1995) (Atluri and Zhu 1998) (Wang and Liu 2002a) (Nguyen et al. 2008) (Belinha 2014).

RPIM present small deviations in the results within the irregular meshes study as the plots of Figure 15 and Figure 14 show.

The radius-thickness ratio studies showed both for clamped and simply supported, the errors are extremely low especially after $R/H \geq 20$.

This extensive series of studies undeniably suggest that RPIM is a robust method and highly suitable to predict any axisymmetric mechanical related phenomenon in linear-elastic regime.

6.2. Rate-Independent Isotropic Damage Model: Plain Concrete

The relevant cumulative nonlinear conditions of a three point bend test of a notched concrete beam is nothing but a sieve for dismiss any 'lucky' results. The detailed and fair study of convergence for the isotropic rate-independent damage law implementation left few doubts, if any, of the fully validation of it. This is clear from Figure 22 where the closer we get from the experimental load-deflection curve as we increase nodal density near the nonlinear area.

The traction stress fields show the expected relaxing effect of highly damaged zones.

The almost perfect vertical narrow zone of damage in Figure 24, resembling a confined crack shape, is coincident with real experimental crack images of beam bend tests, Figure 23. This is also in agreement with damage fields presented by other authors (Voyiadjis and Taqieddin 2009).

The highly severe irregular nodal meshes imposed in ten randomly distinct trials show a narrow strip zone trend, of the load deflection in Figure 31. That thin 'curve-zone' area show an undeniable stable robust behavior of damage model implementation despite far from ideal nodal disposals.

6.3. Rate-Independent Isotropic damage Model: Reinforced Concrete

The damage laws in the context of a four point bend test of a reinforced concrete beam, present an added control over the already validated model. This test results can be viewed as even more relevant than the previously example. The added complexity of inclusion of two material types in three different areas of the model is magnified with the distinct nonlinear material evolution laws for them. The load-deflection curve, Figure 36, show remarkable low profile deviations, from experimental, either in value as in shape.

Despite the traction damage field shows a particular unexpected, wide damaged area, that is not necessarily incompatible with the cracked area in the images of the real tests, Figure 37 and Figure 38. At same time, even Figure 37 shows anything but a 'perfectly' symmetric crack pattern. But we may conclude, that behavior apparently suggests this model implementation needs further improvement to capture an explicit crack evolution.

Still regarding the crack prediction, the Figure 40 shows agreement with the most pronounced left 45^{o} crack of Figure 37. Traction strain field, Figure 40, proved to be a very useful tool to make such predictions. This is much noticed in the reinforced beam example because even the displacement field, Figure 43, lacks of evidence of any signs of crack. This was distinct from the plain concrete example where both strain field, Figure 25 and displacement field where equally 'crack evidence' predictors.

The reinforced example led to, beyond compression yield stress, evolution law to be activated to some relevant area extent. The compression damage field zone, at top of the beam, in Figure 39 is compatible with the horizontal cracked zone at the top of the beam in Figure 37.

This last example fully validates (or 'double' validates) the implementation of damage model within this work.

References

Atluri, S. N., and T. Zhu. 1998. “A New Meshless Local Petrov-Galerkin (MLPG) Approach in Computational Mechanics.” *Computational Mechanics* 22 (2): 117–27. doi:10.1007/s004660050346.

Bathe, K. 1982. *Finite Element Procedures in Engineering Analysis*. New Jersey: Prentice-Hall, Inc.

Bazant, Zdenek P. 2010. “Can Multiscale-Multiphysics Methods Predict Softening Damage and Structural Failure?” *International Journal for Multiscale Computational Engineering*. doi:10.1615/IntJMultCompEng.v8.i1.50.

Belinha, J. 2014. *Meshless Methods in Biomechanics - Bone Tissue Remodelling Analysis*. Edited by J.M.R.S. Tavares and R.M. Natal Jorge. Vol.16 ed. Lecture Notes in Computational Vision and Biomechanics, Springer Netherlands.

Belytschko, T., Y. Y. Lu, and L. Gu. 1994. “Element-Free Galerkin Methods.” *International Journal for Numerical Methods in Engineering* 37 (2): 229–56. doi:10.1002/nme.1620370205.

Cervera, M, J Oliver, and O Manzoli. 1996. “A Rate-Dependent Isotropic Damage Model for the Seismic Analysis of Concrete Dams.” *Earthquake Eng & Struct Dynamics* \textbf{25 (April): 987–1010. doi:10.1002/(SICI)1096-9845(199609)25:9<987::AID-EQE599>3.0.CO;2-X.

Dinis, L. M J S, R. M. Natal Jorge, and J. Belinha. 2008. “Analysis of Plates and Laminates Using the Natural Neighbour Radial Point Interpolation Method.” *Engineering Analysis with Boundary Elements* 32 (3): 267–79.

Dinis, L.M.J.S., R.M. Natal Jorge, and J. Belinha. 2007. “Analysis of 3D Solids Using the Natural Neighbour Radial Point Interpolation Method.” *Computer Methods in Applied Mechanics and Engineering* 196 (13-16): 2009–28. doi:10.1016/j.cma.2006.11.002.

Farahani, Behzad V., José M. V. Berardo, Rafał Drgas, José César de Sá, António Ferreira, and Jorge Belinha. 2015. “The Axisymmetric Analysis Of Circular Plates

Using The Radial Point Interpolation Method." *Submitted to International Journal for Computational Methods in Engineering Science & Mechanics*.

Faria, R., J. Oliver, and M. Cervera. 1998. "A Strain-Based Plastic Viscous-Damage Model for Massive Concrete Structures." *International Journal of Solids and Structures* 35 (14): 1533–58. doi:10.1016/S0020-7683(97)00119-4.

J. Malvar, G. Warren. 1988. "Fracture Energy for Three-Point Bend Tests on Single-Edge Notched Beams." *Naval Civil Engineering Laboratory*, no. March: 1–28. doi:10.1007/BF02329022.

Liu, Gr, and D Karamanlidis. 2003. "Mesh Free Methods: Moving Beyond the Finite Element Method." *Applied Mechanics Reviews*. doi:10.1115/1.1553432.

Liu, Wing Kam, Sukky Jun, and Yi Fei Zhang. 1995. "Reproducing Kernel Particle Methods." *International Journal for Numerical Methods in Fluids* 20 (8-9): 1081–1106. doi:10.1002/fld.1650200824.

Metwally, Ibrahim M. 2015. "Three-Dimensional Nonlinear Finite Element Analysis of Concrete Deep Beam Reinforced with GFRP Bars." *HBRC Journal*. Housing and Building National Research Center. doi:10.1016/j.hbrcj.2015.02.006.

Nguyen, Vinh Phu, Timon Rabczuk, Stéphane Bordas, and Marc Duflot. 2008. "Meshless Methods: A Review and Computer Implementation Aspects." *Mathematics and Computers in Simulation* 79 (3): 763–813. doi:10.1016/j.matcom.2008.01.003.

Polanco-Loria, M., and S. I. S¢rensen. 1995. "Fracture Mechanics of Concrete Structures, Proceedings FRAMCOS-2, Edited by Folker H. Wittmann, AEDIFICATIO Publishers, D-79104 Freiburg (1995)," 1027–36.

Segall, Paul. 1992. "Axisymmetric Reservoirs." *Pageoph* 139 (3): 535–60. doi:10.1007/BF00879950.

Timoshenko, Stephen, and S. Woinowsky-Krieger. n.d. *Theory of Plates and Shells*. 2sd ed. New York: McGraw-Hill International Editions.

Voyiadjis, Gz, and Zn Taqieddin. 2009. "Elastic Plastic and Damage Model for Concrete Materials: Part I-Theoretical Formulation." *International Journal of Structural Changes in Solids* 1 (1): 31–59. https://journals.tdl.org/IJSCS/article/view/2313/0.

Wang, J. G., and G. R. Liu. 2002a. "A Point Interpolation Meshless Method Based on Radial Basis Functions." *International Journal for Numerical Methods in Engineering* 54 (11): 1623–48. doi:10.1002/nme.489.

Wang, J.G., and G.R. Liu. 2002b. "On the Optimal Shape Parameters of Radial Basis Functions Used for 2-D Meshless Methods." *Computer Methods in Applied*

Mechanics and Engineering 191 (23-24): 2611–30. doi:10.1016/S0045-7825(01)00419-4.

Wang, J.G., G.R. Liu, and Y.G. Wu. 2001. “A Point Interpolation Method for Simulating Dissipation Process of Consolidation.” *Computer Methods in Applied Mechanics and Engineering* 190 (45): 5907–22. doi:10.1016/S0045-7825(01)00204-3.

Zienkiewicz, O.C., and R.L. Taylor. 1994. *The Finite Element Method*. 4th ed. London: McGraw-Hill.